arXiv:physics/0406134v1 [physics.optics] 26 Jun 2004

2-d Microcavities: Theory and Experiments *

Jens U. Nöckel
Department of Physics
University of Oregon, Eugene, OR 97403-1274
darkwing.uoregon.edu/~noeckel

Richard K. Chang
Department of Applied Physics
Yale University, New Haven, CT 06520
http://www.eng.yale.edu/rkclab/home.htm

2nd February 2008

An overview is provided over the physics of dielectric microcavities with non-paraxial mode structure; examples are microdroplets and edge-emitting semiconductor microlasers. Particular attention is given to cavities in which two spatial degrees of freedom are coupled via the boundary geometry. This generally necessitates numerical computations to obtain the electromagnetic cavity fields, and hence intuitive understanding becomes difficult. However, as in paraxial optics, the ray picture shows explanatory and predictive strength that can guide the design of microcavities. To understand the ray-wave connection in such asymmetric resonant cavities, methods from chaotic dynamics are required.

*Contribution for *Cavity-Enhanced Spectroscopies*, edited by Roger D. van Zee and John P. Looney (a volume of Experimental Methods in the Physical Sciences), Academic Press, San Diego, 2002

Contents

1 Introduction 3

2 Dielectric microcavities as high-quality resonators 4

3 Whispering-gallery modes 7

4 Scattering resonances and quasibound states 8

5 Cavity ring-down and light emission 11

6 Wigner delay time and the density of states 12

7 Lifetime versus linewidth in experiments 15

8 How many modes does a cavity support? 16

9 Cavities without chaos 18

10 Chaotic cavities 21

11 Phase space representation with Poincaré sections 22

12 Uncertainty principle 23

13 Husimi projection 24

14 Constructive interference with chaotic rays 27

15 Chaotic whispering-gallery modes 28

16 Dynamical eclipsing 30

17 Conclusions 31

1 Introduction

Maxwell's equations of electrodynamics exemplify how the beauty of a theory is captured in the formal simplicity of its fundamental equations. Precisely for this reason, they also illustrate that physical insight cannot be gleaned from the defining equations of a theory *per se* unless we understand how these equations are solved in practice. In optics, one powerful approach to this challenge is the *short-wavelength approximation* leading to the ray picture. Rays are the solutions to Fermat's variational principle, which in particular implies the laws of reflection and refraction at dielectric interfaces. As soon as one makes the transition from wave physics to this classical domain, concepts such as "trajectory", "phase space" and "diffusion" become meaningful. In this chapter, special attention will be devoted to the classical phenomenon of *chaos* in the ray dynamics of small optical cavities, i.e., a sensitive dependence of the ray traces on initial conditions. The main implication for the corresponding wave equation is that it cannot be reduced to a set of mutually independent ordinary differential equations, e.g., by separation of variables. Even when only a few degrees of freedom are present in the system, their coupling then makes it impossible to label the wave solutions by a complete set of "quantum numbers" (e.g., longitudinal and transverse mode numbers). Such a problem is called non-integrable; this classification is due to Poincaré and applies both to rays and waves [1]. Integrable systems are characterized by a complete set of "good quantum numbers", as will be illustrated in section 9

Microcavities can be broadly categorized into active (light emitting) and passive systems. In *active* devices, such as lasers, radiation is generated within the cavity medium, without any incident radiation at the same frequency; the cavity provides feedback and (in combination with a gain medium) sets the emission wavelength [2]. Some of the important properties that characterize a light emitting cavity are emission spectra, emission directivity, output energy, noise properties and lasing thresholds. Examples for *passive* systems are filters, multiplexers and other wavelength-selective optical components; their functionality relies on coupling to waveguides or freely propagating waves in their vicinity. To characterize and operate passive cavities, one is interested in transmission and reflection coefficients, i.e., in the resonator as a scatterer.

The two basic types of experiment, emission and scattering, for a given cavity geometry are intimately connected because they both probe its *mode structure*. The concept of *modes* in microcavities will be made more precise in section 8; as a working definition, let us denote as modes all electromagnetic excitations of the cavity which show up as peak structure in scattering or emission spectra and are caused by constructive interference in the resonator.

Nonintegrable cavities introduce added freedom into the design of novel optical components, especially when we apply results from the field of *quantum chaos*, in which modern quasiclassical methods are of central importance [3, 4, 5, 6, 7, 8, 9]. The term "quantum" in "quantum chaos" relates to the fact that cavity modes are discrete as a consequence of the constructive interference requirement mentioned above; the term "chaos" refers to a degree of complexity in the ray picture which renders inapplicable all simple quantization schemes such as the paraxial method.

The optics problem we are addressing is not one of "quantum optics", but of the quantized (i.e., discrete) states of classical electrodynamics in spatially confined media. *By quasiclassics, we therefore mean the short-wavelength treatment of the classical electromagnetic field.* Confusion should be avoided between quasiclassics as defined here, and the semiclassical treatment of light in the matter-field interaction, which couples quantum particles to the electromagnetic field via the classical (vector) potentials: how we *obtain* the modes of a cavity (e.g., quasiclassically), should be distinguished from how we *use* them (e.g., as a basis in quantum optical calculations). Our main emphasis in this chapter will be on the "how" part of the problem, but the wealth of physics contained in these modes themselves points to novel applications as well. Having made this clarification, we henceforth use the term "semiclassics" synonymously with "quasiclassics" as defined above.

2 Dielectric microcavities as high-quality resonators

Many of the microcavities which are the subject of this chapter employ "mirrors" of a simple but efficient type: totally reflecting abrupt dielectric interfaces between a dielectric body and a surrounding lower-index medium. Resonators occurring in nature, such as droplets or microcrystals, use this mechanism to trap light. This allows us to draw parallels between nature and a variety of technologically relevant resonator designs that are based on the same confinement principle. A recurring theme in numerous systems is the combination of *total internal reflection* (TIR) with a special type of internal trajectory that skips along the boundary close to grazing incidence: the "whispering-gallery" (WG) phenomenon, named after an acoustic analogue in which sound propagates close to the curved walls of a circular hall without being audible in its center [10, 11]. An example for the use of the WG effect in *cavity ring-down spectroscopy* is reported in Ref. [12]. A WG cavity can provide the low loss needed to reduce noise and improve resolution in the detection of trace species; the trace chemicals are located outside the cavity and couple to the internal field by *frustrated total internal reflection*, or evanescent fields. In this section, we review Fresnel's formulas before introducing the WG modes. This provides the basis for sections 9 - 16

In the ray picture, the Fresnel reflectivity, $R_{Fresnel}$, of a dielectric interface depends on the angle of incidence χ (which we measure with respect to the surface normal) and relative refractive index n. In particular, $R_{Fresnel}$ drops significantly below the critical angle for total internal reflection,

$$\chi_{\mathrm{TIR}} \equiv \arcsin \frac{1}{n}. \tag{1}$$

In the limit of normal incidence on a plane dielectric interface, the reflectivity becomes independent of polarization,

$$R_{Fresnel} = \left(\frac{n-1}{n+1} \right)^2 . \tag{2}$$

If the electric field is polarized perpendicular to the plane of incidence (we shall denote this as transverse magnetic, TM, polarization), then Eq. (2) constitutes the lower bound for the reflectivity. Hence, the limit of a closed cavity is approached with increasing refractive index of the cavity. If, on the other hand, the electric field lies in the plane of incidence (TE polarization), then the reflectivity drops to zero at the *Brewster angle*,

$$\chi_B = \arcsin \frac{1}{\sqrt{1+n^2}}, \tag{3}$$

and thus the closed-cavity limit is never fully reached. Because $\chi_B < \chi_{\rm TIR}$, the polarization does not affect the trapping of light at incident angles $\chi > \chi_{\rm TIR}$ (to leading order in frequency). In addition, because the wavelength λ does not enter the Fresnel formulas, internal reflection can be classified as a "classical" phenomenon which can be understood based on Fermat's principle.

This should be contrasted with the intrinsic frequency dependence of Bragg reflection – the other widespread mechanism for confining light in dielectrics. From an engineering point of view, Bragg reflectors are challenging to realize for lateral confinement. In particular for low-index materials, high-reflectivity windows (stop bands) are direction-*and* frequency dependent with narrow bandwidth. TIR, on the other hand, is broad-band and technologically simple.

At higher orders of λ, wavelength-dependent corrections to Fresnel's formulas do arise because TIR is truly total only for a plane wave incident on an infinite and flat interface. The latter does not hold for boundaries with finite curvature or even sharp corners, and similarly in cases where the incident beam has curved wavefronts, as in a Gaussian beam [13, 14, 15, 16]. The physical reason for radiation leakage in these situations is that light *penetrates* the dielectric interface to some distance which depends exponentially on λ, as in quantum-mechanical tunneling. This allows coupling to the radiation field outside the cavity [13, 14].

The analogy to quantum mechanics rests on the similarity between the Schrödinger and the Helmholtz equation for the field ψ,

$$\nabla^2\psi + n^2(\mathbf{r})k^2\psi = 0 \tag{4}$$

to which Maxwell's equations often reduce. Here, $n(\mathbf{r})$ is the index profile and k the free-space wavenumber. The WGMs of a circular resonator are straightforward to calculate exactly, because the Helmholtz equation separates in cylinder coordinates r, ϕ, z. The circular cylinder and sphere are the two main representatives of this small class [7, 17] of integrable dielectric scattering problems. The analytic solution, due to Lorentz and Mie, of Maxwell's vector wave equations for a dielectric sphere, has a long history [17, 18, 19, 20, 13, 14]). It finds application in a wide range of different optical processes, ranging from elastic scattering by droplets to nonlinear optics [25] and to cavity quantum electrodynamics [21, 22, 23]. Similarly, dielectric cylinders are used, e.g., as models for atmospheric ice particles [24] or edge-emitting microdisk and micropillar lasers [26, 27, 28]. Because of rotational symmetry, the ray motion in a sphere is always confined to a fixed plane. By contrast, rays in a cylinder can spiral along the axis [29, 30], but the

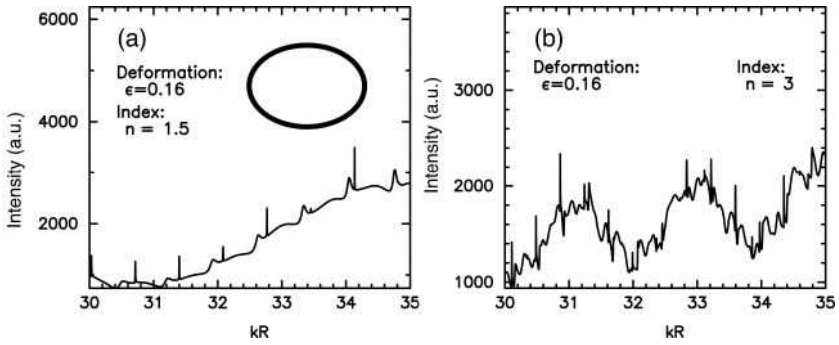

Figure 1: Light scattering spectra for a resonator in the shape of an ellipse with eccentricity $e = 0.8$, defined in terms of the major and minor axes a, b as $e = \sqrt{1-(b/a)^2}$. The length scale $R \equiv \sqrt{ab}$ is used in our calculations to convert the wavenumber into the dimensionless "size parameter" kR. The index of refraction is $n = 1.5$ in (a) and $n = 3$ in (b), showing how the openness of a dielectric cavity increases when n is reduced. The incoming plane wave in (a) and (b) travels parallel to the major axis, and the scattered intensity is detected at 90° from incidence.

propagation becomes planar if the incident wave is aligned to be perpendicular to the cylinder axis. Similar symmetry arguments make it possible to find analytic solutions in concentrically layered dielectrics or ring resonators [31, 32, 33].

Each time a degree of freedom can be separated due to symmetry, the effective dimensionality of the remaining wave equation is reduced by one – in the above examples one finally arrives at an ordinary (one dimensional) equation for the radial coordinate. Even without symmetry properties such as in the sphere or cylinder, one often finds approximate treatments by which such a reduction from three to fewer dimensions can be justified: in fact, in *integrated optics*, most functions are performed by planar optical devices, for which the mode profile in the vertical direction can be approximately separated from the wave equation in the horizontal plane, leaving a two-dimensional problem. For a discussion of methods exploiting this assumption (e.g. the effective-index method), the reader is referred to the literature [34].

One of the advantages of reducing the cavity problem to two degrees of freedom is that polarizations can approximately be decoupled into TE and TM. The resulting wave equations are then scalar, with the polarization information residing in the continuity conditions imposed on the fields at dielectric interfaces. Therefore, the fields are formally obtained as solutions of Eq. (4) in two dimensions. This scalar problem is the starting point for our analysis. In the absence of absorption or amplification, the index $n(\mathbf{r})$ which defines our microcavity is real-valued, and approaches a constant (taken here as $n = 1$ for air) outside some finite three-dimensional domain corresponding to the cavity.

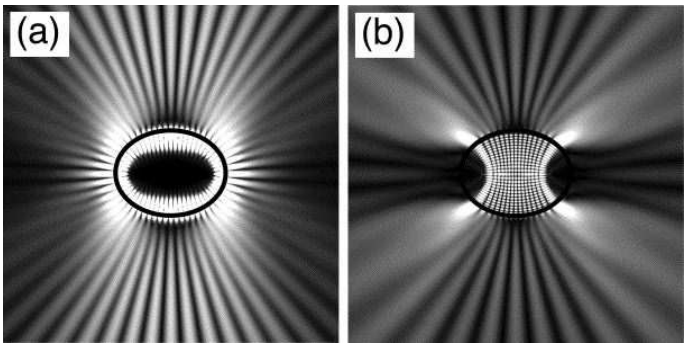

Figure 2: Numerical solution of Maxwell's equations for the internal and external intensity of TM modes in an elliptic cylinder with a refractive index of $n = 1.5$ (a) and $n = 3$ (b), respectively (assuming $n = 1$ on the outside). The eccentricity is $e = 0.709$ in both plots. The dimensionless wavenumber in (a) is $kR = 21.27636$ at a resonance width of $\kappa R = 0.0085$; the state in (b) is found at $kR = 20.69345$ and has a width of $\kappa R = 0.05$. The grayscale shows high intensity as white.

3 Whispering-gallery modes

Figure 1 illustrates the formation of whispering-gallery modes (WGMs) for a dielectric ellipse illuminated by a TM polarized plane wave. The wavenumber k is made dimensionless by multiplying with the mean radius R of the two-dimensional shape. The sharp features in the spectra of Fig. 1 are caused by modes which rely on Fresnel reflection. This can be deduced from the fact that the spectrum becomes more crowded as the refractive index is doubled from $n = 1.5$ (a) to $n = 3$ (b); the intuitive reasoning is that a larger set of ray paths acquires high reflectivity as n increases. The more regularly spaced peaks of Fig. 1 (a) can in fact be identified as WGMs: Light circumnavigates the perimeter of the cavity in such a way as to insure TIR during a complete round-trip, i.e., $\chi > \chi_{\mathrm{TIR}}$ at all encounters with the boundary. Consequently, long-lived cavity modes can form by constructive interference. In the stability diagram of linear paraxial resonator theory [2], a circular dielectric WG cavity could be classified as a confocal resonator with closed but leaky mirrors. Gaussian-beam paraxial optics fails in circular cavities because the beam parameters become undefined in the confocal limit.

The Mie treatment of circular and spherical micro-objects may serve as starting points for *perturbative* treatments of resonators whose shape deviates only slightly from rotational symmetry [35], or when objects in the vicinity of the cavity exert a weak influence [36]. Perturbation methods are among the most powerful tools of wave physics, but one must be aware that there are phenomena outside their reach (most apparent when energy denominators diverge). As a simple example, we return to the elliptical resonator [37]. If we assume impenetrable boundaries (of Dirichlet type), it is a classic textbook problem [38] to obtain the WGMs of the ellipse by applying perturbation theory to a circular cavity. The weakness of this approach is revealed when we recall that the modes can be found by an exact separation of variables and fall into two classes: WGMs and

beam-like "bouncing-ball" states; in Fig. 2 we illustrate these two classes with slightly more complicated dielectric boundary conditions. Since bouncing-ball modes do not *exist* in the circle, perturbative expansions for this type of modes can be expected to become problematic, especially when attempting to describe how some modes of the circle lose their WG character under a continuous shape deformation.

The wave solutions shown in Fig. 2 show field intensity extending to the exterior of the cavity because the dielectric interface is "leaky". In general, such a calculation must be performed numerically; we shall discuss the definition and emission properties of these *leaky modes* further below, in section 4 For now, we are only concerned with the internal intensity patterns. The reader will recognize a strong similarity between the "bouncing-ball" mode and a higher-order transverse Gauss-Hermite beam; this arises because the ray motion corresponding to this mode is a stable oscillation between the flat sides of the cavity. The analytic transverse form of the bouncing-ball beam in the ellipse is however not a Gaussian, but a Mathieu function. The caption of Fig. 2 gives the *linewidth* κ of the two types of modes, indicating that the WG resonance is almost an order of magnitude narrower than the bouncing-ball mode, *despite* the twofold higher refractive index used in Fig. 2 (b).

The ellipse has been chosen as an example because it is integrable in the limit of no leakage. Other oval deformations of the circle do not have this simplifying property. However, families of WG ray trajectories have been proven [39] to exist in any sufficiently smooth and oval enclosure, provided that its curvature is nowhere zero. This makes WGMs a very robust phenomenon of general convex oval cavities. Before we discuss in more detail the relation between the ray picture and the internal structure of the resonator modes, we now turn to some general considerations on what allows us to define the modes of an open cavity.

4 Scattering resonances and quasibound states

WGMs are not infinitely long-lived even in an ideal dielectric cavity, as we saw in the finite linewidths of Fig. 1. In fact, for a finite, three-dimensionally confined dielectric body, all solutions to Eq. (4) are extended to infinity, forming a continuous spectrum. A basis of eigenfunctions is given by the *scattering states*, consisting of an incoming wave ψ_{in} that is elastically scattered by the dielectric microstructure of index $n(\mathbf{r})$ into an outgoing wave ψ_{out}. In the asymptotic region where $n = 1$, the relation between incoming and outgoing waves is mediated by the *scattering operator* S, known from quantum scattering theory [40], to which the electromagnetic resonator problem is conceptually analogous. The S-matrix formalism has long been in use in microwave technology as well as optics [41]: A matrix representation is obtained by defining basis states $|\nu\rangle$ ($|\mu\rangle$) in which the asymptotic incoming (resp., outgoing) fields can be expanded; one has

$$\begin{aligned} \psi_{scat} &= \psi_{in} + \psi_{out}, \\ \langle \mu | \psi_{out} \rangle &= \sum_{\nu=1}^{M} S_{\mu\nu} \langle \nu | \psi_{in} \rangle. \end{aligned} \tag{5}$$

Here, S is a unitary matrix if the incoming and outgoing waves are normalized to carry unit flux, and if $n(\mathbf{r})$ is real. The dimension M is the number of open scattering channels; in the Fabry-Perot cavity there are two channels: both, the incident field $|n\rangle$ and the outgoing states $|m\rangle$ can be a plane wave either traveling on the *left* or on the *right* of the cavity. In 2D and 3D, it is often useful to use angular momentum eigenstates as the basis defining the channels.

Only the properties of the index profile, not of the particular incoming wave, enter S. For a review of scattering theory see, e.g., [42]. As was seen in Fig. 1, the actual *cavity modes* in this continuum of scattering states are revealed if we measure the scattering of light as a function of wavenumber k. The amplitude of the scattered field shows resonant structure at discrete values of k which do not depend on the detailed spatial form of the exciting field ψ_{in}. These resonances are caused by poles of S in the complex k plane, and are a characteristic of the microcavity itself. In Eq. (5), we note that a pole of S admits nonvanishing ψ_{out} in the absence of any incoming waves, $\psi_{in} = 0$. In these solutions at complex k, also known as the quasibound states, we have finally found a proper definition of what we simply called "cavity modes" earlier.

A well-known example is the linear two-mirror (Fabry-Perot) cavity [2]. Its resonances are easily obtained within physical optics by writing the transmission of an incident ray as a geometric series over multiple *round trips*. In each round trip, the amplitude of a ray in the cavity accrues a factor $r_1 r_2 \exp(i\,n\,k\,\ell + i\,\phi_1 + i\,\phi_2)$, where ℓ is the round-trip path length. We have split the amplitude reflectivities at the individual reflections $\nu = 1,\, 2$ into modulus r_ν and phase ϕ_ν. Attenuation comes from $r_\nu < 1$ ($\nu = 1,\, 2$ in the two-mirror case). The refractive index n in the cavity is real, as stated below Eq. (4), and the wave number k is measured in free space. The transmitted amplitude T_{total} is obtained by summing this over all repetitions,

$$T_{total} = I \sum_{\sigma=1}^{\infty} \left(r_1\, r_2\, e^{i\,n\,k\,\ell + i\,\phi_1 + i\,\phi_2} \right)^{\sigma}, \tag{6}$$

where the prefactor I is determined by the incident wave and the mirror transmittivities. This geometric series can be summed, leading to a denominator $1 - \tilde{g}_{\rm rt}(\tilde{\omega})$, with the round-trip "gain"

$$\tilde{g}_{\rm rt}(\tilde{\omega}) = e^{in\tilde{\omega}\ell/c} \prod_{\nu} r_\nu\, e^{i\phi_\nu}. \tag{7}$$

In our example, ν runs from 1 to 2. Whenever $\tilde{g}_{\rm rt}$ comes close to 1, the resonator exhibits a transmission peak. The equality $\tilde{g}_{\rm rt}(\tilde{\omega}) = 1$ can be satisfied only if we admit complex frequencies, $\tilde{\omega} \equiv \omega + i\gamma$, and choose for the imaginary part

$$\gamma = -\frac{c}{\ell} \sum_{\nu} \ln r_\nu. \tag{8}$$

On the real frequency axis, γ determines the resonance linewidth. Were we to look at the complex-frequency solution directly and reinstate the time dependent factor $\exp(i\,\tilde{\omega}t)$ that accompanied the original wave equation, the field at every point in space would decay with a factor $\exp(-\gamma t)$. An interpretation of this can be given in the ray picture:

for a ray launched *inside* the cavity, the field is attenuated by a factor $r_1\, r_2$ in each round trip; after time t, the number of round trips is ct/ℓ, leading to the exponential law

$$E(t) = e^{ct\ln(\Pi r_\nu)/\ell} = e^{-\gamma t}. \tag{9}$$

Hence, each transmission peak is uniquely associated with a metastable, or *quasibound* state, and the decay rate is determined by the reflectivities encountered during a round trip.

Equation (9) straightforwardly justifies the concept of a metastable state within the ray picture. We introduced resonances as peaks in the transmitted field, arising as near-divergences of a geometric series over ray paths undergoing multiple reflections inside the cavity. This is in fact just a special case of a very general quasiclassical approach which has found widespread use in chemical physics [43] and other fields [44] since its original introduction by Miller [6, 45]. It relates the S-matrix element between arbitrary channels μ and ν of a multichannel scattering process to a sum over all possible ray paths starting in channel ν and ending in μ:

$$S_{\mu\nu} = \sum_\sigma \sqrt{p_{\mu\nu}^{(\sigma)}}\, \exp\left(ik\,\Phi^{(\sigma)} - i\alpha^{(\sigma)}\right), \tag{10}$$

where σ parameterizes the family of ray trajectories leading from incoming channel ν to outgoing channel μ, just as in Eq. (6). $\alpha^{(\sigma)}$ is a phase shift acquired by the rays as they encounter caustics and interface reflections along their path. The phase shift $k\Phi^{(\sigma)}$ is the generalization of the dynamical phase $k\,\ell$ in the linear example, and $p_{\mu\nu}^{(\sigma)}$ is the transition probability, corresponding to the product of reflection and transmission coefficients in our two-mirror example. For a cavity defined by Fresnel reflection, $p_{\mu\nu}^{(\sigma)}$ can to lowest approximation be determined purely within ray optics.

The virtue of Eq. (10) is that it points the way from geometric optics to wave optics even in systems where the ray paths are not as easily enumerated as in the Fabry-Perot cavity. The Fabry-Perot cavity discussed above is an example where Eq. (10) in fact yields exact results, because only plane-wave propagation is involved. Although corrections to this quasiclassical formula are necessary in more complicated cavity geometries, Eq. (10) makes it plausible that ray considerations are a powerful tool for understanding quasibound states in many open systems. In this spirit of ray-based scattering theory, we can ask how to extract the *quasibound states* as poles of the physical-optics expression Eq. (10). This means we want to generalize the logical transition (illustrated for the Fabry-Perot cavity) from a transmission amplitude determined by Eq. (7) to an internal ray loop with attenuation given by Eq. (9). Thus, the original scattering problem should be replaced by a Monte-Carlo simulation of a suitable ensemble of rays *inside the resonator*, and the internal ray dynamics suffers *dissipation* owing to the openness of the cavity. Several technical problems make it difficult to carry out this idea in a general cavity: the first question is what would be the proper choice of initial conditions for a ray ensemble in a two-dimensional cavity such as the ellipse of Fig. 2. The answer is provided by quasiclassical quantization conditions that put some constraint on the ray paths to be used in the ray calculation. Employing a strategy along these lines, it is

possible to predict not only the decay rate of a quasibound state as in Eq. (9), but also the *directionality* of the emitted radiation [51]. This will be expounded in sections 11 and 14

5 Cavity ring-down and light emission

We now discuss the significance of complex frequencies in Eqs. (4) and (5). This will highlight the relation between quasibound states and the observable cavity response to an external field or pump signal, which is of particular interest in spectroscopy. In Eq. (4), the wavenumber only appears in the form of a product $n\,k$, so that an imaginary part in $\tilde{k} \equiv k + i\kappa \equiv \tilde{\omega}/c$ can immediately be re-interpreted as part of a complex refractive index $\tilde{n}$ at *real* k, setting

$$n\,\tilde{k} \equiv n\,(k + i\kappa) = k\,(n + i\,n\kappa/k) \equiv \tilde{n}\,k. \tag{11}$$

The resulting Helmholtz equation has a real wavenumber, and thus describes the steady-state wave solutions in an amplifying medium, because $\kappa > 0$: a plane wave would have the form $\exp(i\omega t - i\tilde{n}kx)$, which grows in the propagation direction. From Eq. (11) it follows that quasibound states appear naturally as approximate solutions for the lasing modes of a microlaser with a homogeneous gain medium [52]. For a physical understanding of lasers [53], the *openness* of the system as contained in the quasibound state description is essential.

When a cavity is excited with a *pulse*, on the other hand, we are not looking for steady-state solutions but for transients. As we noted below Eq. (9), quasibound states describe such a decay process. These non-stationary states are exploited in many fields, e.g. nuclear physics (where they are called "Gamov states"), and their properties are well-known [54, 55]. One peculiar property that may cause confusion is that they formally *diverge* in the far field, as can be seen by noting that the outgoing wave in Eq. (5) obeys the radiation boundary condition, which in the continuation to complex frequency reads

$$\psi_{out} \propto e^{i(\tilde{\omega}t - \tilde{k}r)} \qquad (r \to \infty). \tag{12}$$

This holds for any dimensionality if r is understood to be the radial coordinate, and algebraic prefactors (which depend on the dimension of the solid angle element) are not considered. At fixed t, the imaginary part κ of $\tilde{k}$ causes exponential growth with r. However, grouping together the exponential dependences on position *and* time, the amplitude of the quasibound state is controlled by the factor

$$e^{-\gamma t + \gamma r/c}. \tag{13}$$

Clearly, this remains constant along the spacetime trajectory $r = ct$. The complex-valuedness of $\tilde{\omega}$ $\tilde{k}$ therefore has nothing unphysical, provided *causality* is taken into account: within the ring-down time $1/\omega$ of the cavity, the maximum distance to which we can extend measurements of the radiated field is of order $R \sim c/\gamma = 1/\kappa$. In this

range, $r < R$, the decaying pre-exponential factors dominate over the exponential r dependence.

Equation (11) represents a level of approximation which does not take microscopic properties of the light-emitting medium into account. However, it forms a starting point which emphasizes the effect of the resonator boundaries on the mode structure from the outset; an effect that becomes essential as the cavity size decreases. If we allow the polarization $\mathbf{P}$, which in Maxwell's wave equation effects the coupling between matter and field, to become a function of position, and possibly acquire a nonlinear dependence on the electric field, then it turns out that the quasibound states of the homogeneous medium, discussed above, are nevertheless a convenient basis in which to describe the emission and mode coupling caused by $\mathbf{P}$. To make this plausible, recall that any given electromagnetic cavity field can be expanded in an integral over the scattering states ψ_{scat} of Eq. (5) as a function of k; these are the "modes of the universe" in the presence of the cavity. To evaluate such an integral, one can extend the integration contour into the complex plane and apply the residue theorem. The integral is then converted to a sum over those k at which the integrand has a pole. But the poles of the scattering states are just the poles of the S matrix, i.e. the quasibound states. For details of these arguments, the reader should see Ref. [54]. The radiation from a source distribution $d(\mathbf{r})$ is obtained directly by summing up those quasibound states which lie in the spectral interval of interest, weighted according to their overlap with the distribution $d(\mathbf{r})$, and with an energy denominator that makes sharp resonances contribute more strongly than broad ones. In particular, for small cavities where the free spectral range is large and the linewidths are small, the emission properties are determined by the spatial form and temporal behavior of *individual quasibound states*.

6 Wigner delay time and the density of states

In spectroscopic applications, the quality Q and finesse F of a cavity are important figures of merit. Conventionally, one defines

$$Q \equiv \frac{k_r}{\kappa}, \quad F \equiv \frac{\mathrm{FSR}}{\kappa}, \tag{14}$$

where FSR is the free spectral range and k_r is the wavenumber of the mode. To decide whether the linewidth of an individual resonance, as given by Eq. (8), is narrow or broad, we can choose as our yardstick the separation between neighboring modes. However, as seen in Fig. 1 (b), this can become rather ambiguous if the spectrum is crowded. A free spectral range is then hard to define, and should be replaced by a continuous function of frequency: the spectral density, or *density of states*, $\rho(k)$. If Q and F were independent of k, then the total number of cavity modes with wavenumber less or equal to k would be $N(k) = k/\mathrm{FSR} = Q/F$. The density of states is the k-dependent generalization of the inverse FSR:

$$N(k) = \int_0^k \rho(k')\, dk'. \tag{15}$$

The structure of $\rho(k)$ contains all the information about both $Q(k)$ and $F(k)$.

For a dielectric scatterer with sharp boundaries, there is in principle a clear distinction between "inside" and "outside". An incoming wave propagates freely outside the dielectric, but can be trapped inside for some time. Therefore, an incident wave pulse emerges from the scatterer with a time delay, τ_D, compared to the time it takes in the absence of the obstacle ($S \equiv 1$). The time delay is a continuous function of k, whereas the resonance decay time $1/\gamma$ labels discrete poles of the S-matrix. To clarify the relation between *delay time* and *decay time*, consider the simplest case of a one-channel scattering system, in which $\psi_{in} \propto \exp(i\omega t + ikx)$ and $\psi_{out} \propto \exp[i\omega t - ikx + i\theta(k)]$. Here, θ is the *scattering phase shift*, which is related to the (unitary) S-matrix of Eq. (5) by

$$S(k) = \exp[i\theta(k)]. \tag{16}$$

The outgoing wavepacket then has the Fourier decomposition

$$\psi(x,t) = \int dk\, \xi(k)\, e^{ik(ct-x)+i\theta(k)}. \tag{17}$$

We can look at this general expression in two instructive limiting cases: the magnitude of of the Fourier spectrum, $|\xi(k)|$, could be assumed to be either sharply peaked or slowly-varying. Consider first the case where $|\xi(k)|$ has a narrow peak at some central wavenumber k_0; the opposite limit will be treated in Eq. (27). Then the variation of θ with k need only be retained to linear order, yielding

$$\theta(k) \approx \theta(k_0) + (k-k_0)\,\frac{d\theta}{dk_0} \quad \Rightarrow \quad \psi(x,t) \approx \text{const} \times \int dk\, \xi(k)\, e^{ik(ct-x+d\theta/dk_0)}. \tag{18}$$

If we denote by $\psi_0(x,t)$ the corresponding pulse for $\theta \equiv 0$, i.e. without scattering, then the last equation means

$$\psi(x,t) = \psi_0\left(x, t + \frac{1}{c}\frac{d\theta}{dk_0}\right). \tag{19}$$

This shift in t is the *Wigner-Smith delay time*, $\tau_D(k)$ [56, 57]; it is a continuous function of k. For or a general scattering system with $M \geq 1$ channels, $\tau_D(k)$ is obtained by adding the k - derivatives of all the phases θ_μ entering the M eigenvalues $\exp(i\theta_\mu)$ of the S matrix:

$$\tau_D(k) \equiv \frac{1}{M\,c}\sum_{\mu=1}^{M}\frac{\partial\theta_\mu}{\partial k} = \frac{i}{c}\,\mathrm{Tr}\left(\frac{dS^\dagger}{dk}S\right) = \frac{1}{c}\,\mathrm{Im}\,\mathrm{Tr}\left(\frac{d}{dk}\ln S(k)\right). \tag{20}$$

The last equality is a matrix identity; it contains a trace over all open channels $\mu = 1 \ldots M$. The logarithmic derivative can be executed immediately if one channel is resonant: near a resonance frequency $\omega_r = ck_r$ one has

$$S \propto 1/(k - k_r - i\kappa) \tag{21}$$

with κ describing the linewidth, or the decay rate in Eq. (13) via $\gamma = c\kappa$. Then

$$\tau_D(k_r) \approx \frac{1}{c\kappa} = \frac{1}{\gamma}, \tag{22}$$

which means that the *resonant* time delay equals the resonance lifetime.

The spectral density of the open system is closely related to the delay time τ_D, as we can understand from the following (non-rigorous) argument (for more stringent derivations, see, e.g., [60]): τ_D defines a *length scale* $L_\tau \equiv c\,\tau_D/n$ (n is the refractive index) which is the characteristic distance over which the wave will propagate inside the scatterer. If we interpret this as the effective "cavity length", then a mode should naively be expected when an integer number of wavelengths fits into this length, i.e.,

$$nk\,L_\tau = 2\,\pi\,\nu + const, \tag{23}$$

where ν is an integer, and the constant takes into account phase shifts at interface reflections or caustics. The number of modes that are contained in a small interval Δk around k is then given by the corresponding change $\Delta\nu$ in the above equation, which to lowest order in k is

$$\Delta\nu = \frac{1}{2\,\pi}\,L_\tau\,n\Delta k. \tag{24}$$

Therefore, the spectral density is simply

$$\rho(k) = \frac{\Delta\nu}{\Delta k} = \frac{n}{2\,\pi}\,L_\tau = \frac{c}{2\,\pi}\tau_D(k) \tag{25}$$

This, combined with Eq. (20), is the *Krein-Friedel-Loyd formula* for the density of states in an open system, which re-appears almost invariably whenever linear response or time-dependent perturbation theory in the presence of a continuous spectrum are considered [58, 59, 60, 61, 62, 63, 64, 65]. An important example is Fermi's golden rule which relates electronic transition rates W to the squared matrix element $|M|^2$ of the interaction and the density of states,

$$W(k) = \frac{2\pi}{\hbar^2}|M|^2\rho(k). \tag{26}$$

Based on this and Eq. (25), we can state that microcavities are able to enhance optical transition rates, because at certain wavenumbers the light is trapped (i.e., delayed) in the cavity for long times.

The density of states is one of the fundamental quantities that make small cavities interesting, as was recognized long ago by Purcell [66, 67, 68, 69, 70, 85] who observed that Eq. (26), when applied to the probability for spontaneous emission, can lead to an enhancement of this atomic decay process compared to its rate in free space, by many orders of magnitude. What we have seen here is that peaks in the spectral density are associated with rapid variations in the S matrix, i.e., with the quasibound states discussed in section 4. Small cavities also enable the opposite effect, a suppression of spontaneous emission when no cavity modes fall within the emission spectrum [68, 71, 72].

The limit of a well-defined frequency in the wavepacket of Eq. (17) allowed us to assume that the radiation interacts only with a single quasibound state, leading to the resonant delay time Eq. (22). On the other hand, if we take $|\xi(k)| \equiv C$ to be constant, the whole spectrum enters with equal weight. One could still make the assumption that

there is only a single isolated resonance in the spectrum; then one immediately arrives at the well-known relation between Lorentzian lineshape and exponential resonance decay: take the resonance to be at wavenumber k_r (it is in fact always accompanied by a partner state [35] at $-k_r$, but we can ignore it at large enough frequencies); replacing $exp(i\theta) = S$ in Eq. (17) by Eq. (21), what remains is the Fourier transform of a Lorentzian,

$$\psi(x,t) = C \int dk \, \frac{1}{k - k_r - i\kappa} e^{ik(ct-x)} \propto e^{-\kappa(ct-x)} e^{ik_r(ct-x)}. \tag{27}$$

This is a damped oscillation as a function of $ct - x$ at frequency $\omega_r = c\,k_r$ with decay constant $\gamma_r = c\kappa_r$. Comparing with Eq. (13), we have recovered the decay law of an individual quasibound state in the field envelope.

According to Eq. (27), if we could make a time-resolved measurement of the oscillating electric field in the outgoing wave, the resonance lifetime would show up in the decaying envelope of the successive peaks of the rapidly oscillating field. It is impractical to make such a measurement at optical frequencies. However, recent advances have been able to approach this limiting case of Eq. (17) by making the wavepackets into ultrashort pulses, where correspondingly $|c(k)|$ becomes very broad. This will be discussed further in the next section. The results of a real experiment are, however, modified from this simple Lorentzian approximation because the scatterer in general supports more than one distinct quasibound state. The Fourier transform in Eq. (17) consequently does not yield a purely exponential envelope, except at long times when the decay is dominated by the narrowest resonance [73].

7 Lifetime versus linewidth in experiments

The two limiting cases of $\xi(k)$ in the wavepacket Eq. (17) are just extremes of the time-frequency uncertainty relation. Experiments on microcavities have been performed both in the spectral and time domain. However, there has been only one report of the temporal nature of an *ultra-short* optical wavepacket (100 fs pulse, 30 m short in air) incident on a pendant-shaped, hanging droplet with an equatorial radius of 520 m [74]. Such pulses are spectrally broad but have the intriguing property that their spatial length is much shorter than the cavity size. Conceptually, the analogy to a well-defined particle trajectory suggests itself, and hence one looks for *ballistic* propagation in the cavity. In the experiment, wavepackets were observed to circulate inside the droplet in the region where the the WGMs reside; such paths are characteristic of high-order rainbows in that entry and exit of the light are separated by a large number of internal reflections [19, 47].

The time-resolved measurement showed that coherent excitation of a large number of WGMs allows propagation of a short wavepacket along the sphere's equator for several round trips without significant decoherence, except for decrease in the wavepacket intensity because of leakage of the WGMs. The novel aspect of the experiment that enabled the time-resolved measurements was the use of two-color two-photon-excited Coumarin 510 dye molecules embedded in the liquid (ethylene glycol) that formed the pendant

droplet. The Coumarin fluorescence (near 510 nm) appears when one wavepacket of λ_1 and another wavepacket of λ_2 spatially overlap. Thus, the Coumarin fluorescence acts as a correlator between wavepackets.

This time-resolved experiment was designed to answer the following questions: (1) does the excitation wavepacket remain intact and ballistic after evanescent coupling with WGMs? (2) after a few round trips, would dispersion cause the wavepacket to broaden? and (3) can the cavity ring down time be observed for those wavepackets that make several round trips? The answers were reached that the shape of excitation wavepacket remained intact, the wavepacket was not broadened after a few round trips, and that cavity ring down was observed for each round trip. This is an extension of the single-mode ring-down determined by Eq. (27).

In particular in the context of cavity ring-down spectroscopy, the usefulness of time-domain measurements is recognized [75]. There, one deals with very high Q-factors and their modification by the sample to be studied. Another application of temporal observation is encountered in microdroplets, where the optical feedback provided by WGMs makes it possible to reach the threshold for stimulated Raman scattering (SRS). The SRS spectrum consists of sharp peaks, commensurate with the higher Q WGMs located within the Raman gain profile. The highest Q value of the WGMs can be determined either by resolving the narrowest linewidth $\Delta\lambda$ of the SRS peak or by measuring the longest exponential decay of the SRS signal after the pump laser pulse is off. When $Q > 10^5$, the decay time $\tau = Q/\omega$ (where $\omega \approx 3 \times 10^{15}$ Hz for $\lambda = 620$ nm) becomes a much easier quantity to measure directly because it is longer than 100 ps. Otherwise, the spectral linewidth ($\Delta\lambda = \lambda/Q$) needs to be resolved better than 0.006 nm (for $\lambda = 600$ nm). Cavity decay lifetimes as long as 6.5 ns have been observed [76].

8 How many modes does a cavity support?

Having defined the density of modes for the open system in section 6, we can go one step further and perform the the *average* $\bar{\rho}(k)$ over some finite spectral interval Δk. The suitable choice for such an averaging interval should of course contain many spectral peaks. Two relevant examples where an average spectral density is of use are the Thomas-Fermi model of the atom [77] and Planck's radiation law. The latter shall serve as a motivation for some further discussion of the average $\bar{\rho}(k)$ in the next section. For a presentation of the subtleties involved in this procedure, cf. Refs. [78, 79]. For our purposes, we simply remark that using Eq. (25) as a starting point, one way of arriving at an averaged spectral density is to make the formal substitution $k \to k + iK$. This amounts to an artificial broadening of all resonances as a function of k to make them overlap into a smoothed function; K then plays the role of the averaging interval [80].

In the limit of the closed cavity, the spectral density becomes a series of Dirac delta functions as the resonance poles move onto the real k axis and become truly bound states. The resonator then defines a Hermitian eigenvalue problem of the type we encounter in all electromagnetics textbooks, and many fundamental properties of realistic cavities can be understood within this lossless approximation. As a point in case, it is worth recalling

the problem of *blackbody radiation*. From a historical point of view, this thermodynamic question was the nemesis of classical mechanics as the foundation of physics, because it led to the postulate of discrete atomic energy levels. From a practical point of view, the blackbody background can be a source of noise in spectroscopic measurements, and its spectrum is modified by the presence or absence of a cavity.

From an *electrodynamic* point of view, the central nontrivial aspect of Planck's problem is that the average spectrum of the blackbody can be observed to be *independent* of the cavity shape. The explanation of this universality rests on the average spectral density of cavity modes, which is found to be independent of the resonator geometry to leading order in frequency. Although it may be intuitively convincing that the shape of the enclosure should become unimportant when its dimensions are large compared to the wavelength [81], the actual proof requires a large measure of ingenuity. In a series of works beginning in 1913 [82], *Weyl* showed that for a closed, three-dimensional electromagnetic resonator of volume V, the average spectral density as a function of wavenumber k is (including polarization)

$$\bar{\rho}^{3D}_{\mathrm{Weyl}}(k) \approx \frac{k^2}{\pi^2} V \quad (\text{in} \quad 3\text{D}), \qquad \bar{\rho}^{2D}_{\mathrm{Weyl}}(k) \approx \frac{k}{2\,\pi} A \quad (\text{in} \quad 2\text{D}). \tag{28}$$

The second equation applies when, as discussed above, the wave equation can be reduced to scalar form and two degrees of freedom for a cavity of area A. The average number of modes in an interval Δk then is $\bar{\rho}_{\mathrm{Weyl}}(k)\,\Delta k$ for large k. Geometric features other than the volume enter in this quantity only as corrections with lower powers of the wavenumber. These terms depend on the boundary conditions, surface area (or circumference) and curvature, as well as on the topology of the cavity [83, 84].

As mentioned in the previous section, Eq. (26), microcavities can lead to enhanced spontaneous emission because of their highly peaked density of electromagnetic modes. Although Weyl's formula is strictly valid only for short wavelengths, it nevertheless allows us to estimate the limiting size for ultrasmall cavities that should be approached if we want to observe such density-of-states effects: note that Eq. (28) approaches a "quantum limit" as the volume V approaches $(\lambda/2)^3$ at fixed wavelength λ: the number of modes with wavenumber below $k = 2\pi/\lambda$ is then

$$\bar{N}^{3D}_{\mathrm{Weyl}}(k) = \int_0^k \bar{\rho}^{3D}_{\mathrm{Weyl}}(k)\, dk \approx \frac{\pi}{3} \approx 1, \tag{29}$$

which means that only a single mode remains in the cavity. In reality, the ultrasmall size approached here is not necessarily the optimal choice, because it is hard to maintain good quality for small cavities. One of the best ways to achieve both small size and long lifetimes is by making use of WGMs in dielectric cavities.

The universality of Weyl's spectral density is surprising if we look at it with the methods of the previous chapter: the analysis for stable resonators [86] shows that the number of modes which can be obtained within the *paraxial approximation* depends strongly on details of the cavity geometry. Recall the nature of the paraxial approximation; it is in

fact a *short-wavelength* approximation to Maxwell's wave equations, in the sense that the characteristic length scale (of the cavity or variations in the refractive-index profile) along the propagation direction must be large compared to the wavelength. In that framework, the *geometric-optics* picture is therefore the backbone on which the mode structure of a cavity is built. However, paraxial modes appear only if *stable*, closed ray patterns exist in the cavity. What makes Weyl's formula nontrivial is that it does not distinguish between a cavity in which such stable orbits are readily available (as was the main subject of the previous chapter), and the extreme yet realizable case of a chaotic cavity in which no stable paths can be found *at all*, see section 10.

Stability is a property of particular rays, not of a cavity as a whole. To understand all the modes of a generic cavity, one has to go beyond paraxiality. It also must be realized that paraxial optics is itself a special case of a more general approximation scheme, known as the *parabolic-equation method* [85, 87]. This name refers to the fact that the resulting wave equation of Schrödinger type is mathematically classified as a parabolic differential equation. This is mentioned here because at a more abstract level, one can build approximations of paraxial type not only around rectilinear rays: e.g., for WGMs, an envelope function ansatz in polar coordinates, $\Psi(r,\,\phi) = \chi(r;\phi)\exp(-i\beta\phi)$ allows ϕ to become the "propagation direction". The question of whether a mode can be called paraxial or not then becomes dependent on the coordinate system one uses (e.g., Cartesian vs. cylindrical). A more *fundamental* distinction by which the cavity as a whole can be classified is that of integrability. Next, we discuss some examples for this concept.

9 Cavities without chaos

One feature that can be observed in both Fig. 2 (a) and (b) is that the modes exhibit *caustics* inside the dielectric, i.e. well-defined curves of high intensity which in the ray picture correspond to envelopes at which the rays are tangent. In the WGM, the caustic is an ellipse *confocal* with the boundary; it can be parameterized by its eccentricity, e_c. In Fig. 2 (b), the caustic consists of two confocal hyperbola segments. Caustics separate the classically allowed from the forbidden regions, in the sense of the WKB approximation. In this section, we discuss some examples of how quasiclassical and exact solutions can be obtained in non-chaotic but nontrivial cavities, if coupling to the exterior region is neglected. In this closed limit, all fields can be written as real-valued functions obeying standard boundary conditions (Dirichlet or Neumann).

Figure 3 (a) illustrates the WG caustics of an ellipse and their relation to the quasiclassical quantization method of Einstein, Brillouin and Keller (EBK, the multidimensional generalization of the WKB approximation) [88]: given a particular caustic of eccentricity e_c, we examine the ray segments that are tangent to it. For a fixed sense of rotation, there are exactly two distinct rays going through any given point $\mathbf{r}$ between the caustic and the boundary – one traveling from the caustic toward the boundary and the other *vice versa*. These two unique ray directions as a function of $\mathbf{r}$ define two vector fields, which are called "ray congruences" [88] and are shown in the figure as a flywheel of rays.

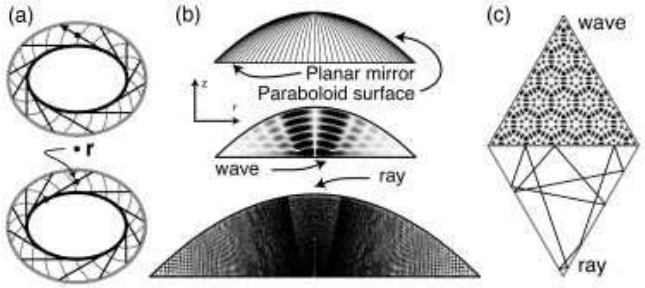

Figure 3: (a) In a WGM of the ellipse, the point $\mathbf{r}$ is visited by two wavefronts: one carrying rays from the caustic to the boundary (top), and the other *vice versa* (bottom); note that both have the same sense of rotation (indicated by the arrow). A complete ray trajectory alternates between these two wavefronts as it encounters boundary and caustic repeatedly. (b) A paraboloid (surface of revolution generated by a parabola), closed by a mirror intersecting its focal point. The focal length equals $3.25\,\lambda$. The azimuthal mode number is $m = 1$; high intensity is shown in black. The corresponding rays (bottom) come in families and generally do not close on themselves (bottom). (c) A 2D equilateral triangle cavity. The side length is $13.5\,\lambda$. The mode can be constructed rigorously from a family of periodic ray orbits, one example of which is shown.

They are furthermore normal to the phase fronts shown as curved grey lines. These are the eikonals $\Phi_{1,2}(\mathbf{r})$ appearing in the quasiclassical ansatz for the wave,

$$\psi(\mathbf{r}) = A_1(\mathbf{r})\,\exp[-i\,k\,\Phi_1(\mathbf{r})] + A_2(\mathbf{r})\,\exp[-i\,k\,\Phi_2(\mathbf{r})] \tag{30}$$

We have suppressed the monochromatic time dependence $\exp(i\omega t)$. At least two terms are necessary when there are two degrees of freedom; additional, symmetry-related terms may be needed to make the wave field real-valued. In the standard EBK quantization, the amplitude functions $A_{1,2}$ are assumed to be slowly varying, and one can achieve the single-valuedness of the wave function only if the phase advance in the exponentials is an integer multiple of $2\,\pi$ for any closed loop in the planar cavity. This occurs only for certain discrete combinations of the unknown parameters k (the wavenumber), and e_c (the eccentricity of the caustic). Hence, the semiclassical method quantizes not only the wave parameter k of the modes, but also the classical parameter e_c defining the corresponding ray trajectories.

A simple example is the *circular resonator*, a limiting case of Fig. 3 (a). The internal caustic in that case is a concentric circle with radius R_i. By geometry, the rays corresponding to that caustic have a fixed angle of incidence given by $\sin\chi = R_i/R$, if R is the cavity radius. Single-valuedness of the wave field then requires that the phase advance along a loop encircling the caustic (= circumference $\times$ wavenumber) equals $2\,\pi\,m$, where m is an integer:

$$2\pi\,R_i\,nk = 2\pi\,m \quad \Rightarrow \quad \sin\chi = \frac{m}{nkR}, \tag{31}$$

where n is the index of refraction. The meaning of m follows if we interpret $p \equiv \hbar n k$ as the linear photon momentum, and recall the definition of classical angular momentum, $\mathbf{L} = \mathbf{r} \times \mathbf{p}$. Then if $\mathbf{r}$ lies on the surface, the z component of $\mathbf{L}$ is $L_z = R p \sin\chi$, which identifies $L_z = \hbar m$ by comparing with Eq. (31). One can thus call m an "angular momentum quantum number". In addition to this orbital angular momentum quantization, there is a radial single-valuedness condition which forces k to become discrete. This yields a complete set of two quantum numbers for two degrees of freedom, and it implies that χ in Eq. (31) becomes discretized as well – another way of understanding the quantization of the caustic e_c. For a basic discussion of the EBK method in rotationally invariant, separable cavity geometries, cf. Ref. [89].

One result of the EBK quantization is that the WGMs do *not* in general correspond to closed ray orbits except in the limit when the internal caustic approaches the cavity surface. The quantized caustics instead belong to a family of rays which encircle the perimeter *quasi-periodically*, coming arbitrarily close to any given point on the boundary after a sufficiently long path length. This generalizes to most other resonator problems: *What counts for the formation of modes is not that the associated rays close on themselves, but only that the wave fronts, to which these rays are normal, interfere constructively.*

Even in three-dimensional integrable cavities, the EBK method can yield highly accurate results down to the lowest-frequency modes. As an example, we mention recent work on a microlaser cavity with strong internal focusing properties, which consists of a dome in the shape of a paraboloid, on top of a layered semiconductor [90], cf. Fig. 3 (b). As in the ellipse, the exact solution for the mode shown for this plano-parabolic mirror geometry bears some resemblance to the more familiar paraxial optics, in this case a Gauss-Laguerre beam. However, just like the circular resonator, the parabolic dome has *no* stable ray orbits, owing to the confocal condition. The modes can be found exactly because the geometry allows separation of variables in parabolic cylinder coordinates.

The short-wavelength approximation can be made highly accurate (as in the parabolic dome) or even *exact* (as in the Fabry-Perot cavity of section 4). As a nontrivial generalization of exact quantization based on rays, Fig. 3 (c) shows the *equilateral triangle*. All its modes can be obtained by superimposing a finite number of suitably chosen plane waves [10, 91, 85]. This is achieved by "unfolding" the cavity into an infinite lattice created by its mirror images. These examples show that ray optics, as the skeleton which carries the wave fields, remains a useful tool far beyond the paraxial limit.

However, the reader may ask: *what is the use for semiclassical methods in exactly solvable problems such as the above systems*? After all, semiclassics is simple in separable systems! Beyond quantitative estimates, the value of quasiclassics is that the connection between modes and rays can be carried over to deformations of the cavity shape where the separability is destroyed. When this happens, eigenstates cannot be labeled uniquely by global quantum numbers anymore. However, as Weyl's formula teaches us, the absence of good quantum numbers does not imply the absence of good modes. In order to classify the latter, we shall attempt to label them according to the ray trajectories to which they quasiclassically correspond.

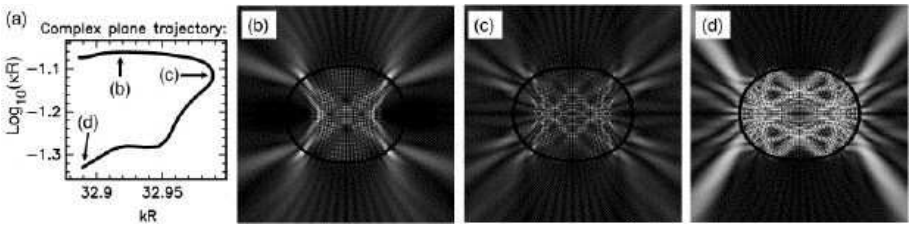

Figure 4: The refractive index in (a-d) is $n = 2.65$. (a) Position $\tilde{k} = k + i\kappa$ of a quasibound state, parameterized by the quadrupolar shape deformation $r(\phi) = R\,(1 + \epsilon\,\cos 2\phi)/\sqrt{1 + \epsilon^2/2}$. Here, ϵ is the fractional deformation from the circle. Arrows show the location of the quasibound states shown in (b-d), corresponding to $\epsilon = 0.114$ (b), $\epsilon = 0.126$ (c) and $\epsilon = 0.135$ (d). The resonance widths are $\kappa R = 0.087, 0.069, 0.047$ in (b), (c), (d). Thus, increasing deformation leads to *linewidth narrowing and more focused emission.*

10 Chaotic cavities

Taken together, the discussions of stable resonators in the previous chapter [86] and of integrable systems in the foregoing section provide the essentials of "conventional" resonator physics. However, in the infinite space of possible cavity shapes, most geometries are nonintegrable and hence display chaos in their ray dynamics, as mentioned in the introduction to this chapter. To illustrate the transition to chaos, Fig. 4 shows the continuous evolution of an individual quasibound state as the shape of an oval resonator is deformed. The cavity shape is a two-dimensional quadrupole of mean radius R. Now the distinction between the mathematical ellipse and other oval shapes becomes important. Although the difference between the shapes in Figs. 4 and 2 is barely discernible at small ϵ, the quadrupole is not an integrable cavity and displays a far more intricate internal mode structure. In particular, caustics become frayed, and nodal lines form ever more complicated patterns as ϵ increases.

Given this complicated scenario, it is not immediately clear that *ray considerations* can help at all in understanding the properties of states such as those in Fig. 4. However, it turns out that quite the opposite is true: it is the added complexity of the internal ray dynamics that can be identified as the *cause* of the more complex wave fields. We make this somewhat provocative statement because the previous examples have proven the success of using ray considerations as a scaffolding for constructing the cavity modes. Unfortunately, there is so far no complete theoretical framework for the quasiclassical quantization of partially chaotic systems; the EBK method, which in quantum mechanics gives rise to the corrected Bohr-Sommerfeld quantization rules [88], fails when the system does not exhibit well-defined caustics, as was already noted by Einstein [92].

However, it is worth following the quasiclassical route because there exists a vast amount of knowledge about the classical part of the problem: chaotic ray dynamics can help gain insights into the wave solutions that cannot be gleaned from numerical computations alone. Ray optics can be formally mapped onto the classical mechanics of a point particle; this allows us to leverage a rich body of work on chaotic classical mechanics

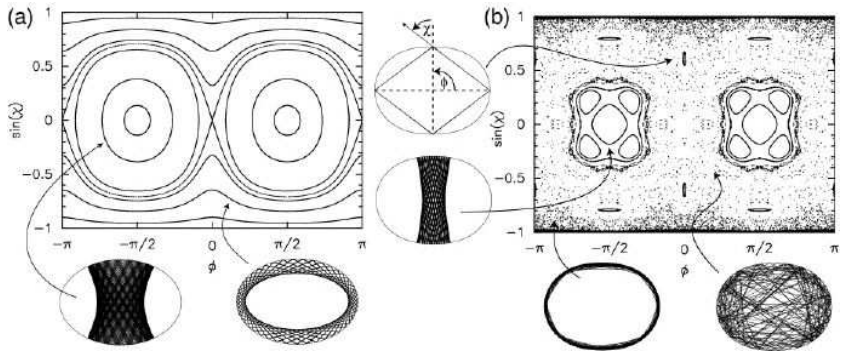

Figure 5: Poincaré surfaces of section: at each reflection, record the position of impact (parameterized by the polar angle ϕ) and angle of incidence χ, in a plot of $\sin\chi$ versus ϕ; repeat for several trajectories. (a) ellipse of eccentricity $e = 0.8$ (same shape as in Fig. 1); (b) quadrupole with $\epsilon = 0.135$, as in Fig. 4 (d). In (a), oscillatory paths between the flat sides appear as closed loops, whereas WG circulation creates curves that span all polar angles ϕ. While all rays in (a) form caustics, the chaotic paths shown in (b) do not. Chaotic rays can undergo WG circulation (bottom left) for long times before covering the whole cavity in a quasi-random way (bottom right).

– a mature, though by no means complete field [1, 5, 93, 94]. Hence, quasiclassics in the presence of chaos is a challenging undertaking, but also a *useful* one because the numerical costs for obtaining exact wave solutions in nonintegrable systems are so high.

As observed in section 7, pulses that excite many cavity modes can behave ballistically, i.e. seem to follow well-defined trajectories. The idea of the quasiclassical approach is complementary to this: from the behavior of whole *families* of ray trajectories, we want to extract the properties of individual cavity modes.

11 Phase space representation with Poincaré sections

As the ellipse already taught us, different types of ray motion can *coexist* in a single resonator – e.g., WG and bouncing-ball trajectories. In such cases, it is desirable to know what combination of initial conditions for a ray will result in which type of motion. Initial conditions can be specified by giving the position on the boundary at which a ray is launched, and the angle χ it forms with the surface normal. The proper choice of initial conditions was identified at the end of section 4 as a prerequisite in the quasiclassical modeling of resonance decay. The present section introduces the tools necessary for solving this problem.

Information on the possible types of ray motion, and how they are grouped in families, is contained in the *Poincaré surface of section* (SOS), cf. Fig. 5. It is a representation of the classical phase space in the ϕ - $\sin\chi$ plane, spanning all possible angles of incidence and reflection positions along the boundary. The definition of χ in the center of Fig. 5 includes a *sign*, measured positive in the direction shown by the arrow from the outward

normal. This reflects the observation made below Eq. (31) that $\sin\chi$ is proportional to the z component of the instantaneous angular momentum at the reflection, and the sign thus distinguishes the sense of rotation.

By combining the two variables ϕ and $\sin\chi$, dynamical structure can be revealed which would remain hidden in a collection of real-space ray traces. Non-chaotic trajectories are confined by local or global conservation laws to one-dimensional lines, called *invariant curves*. Almost all rays in the ellipse follow such curves, as seen in Fig. 5 (a), which shows a clearcut division into oscillatory and rotational (WG) motion, cf. also Fig. 2. This is analogous to the phase space of a physical pendulum [95]. The separatrix between the two types of motion corresponds to a diametral ray orbit connecting the points $\phi = 0,\ \pi$ on the boundary.

Rays launched on an invariant curve must remain on it for all subsequent reflections. Such unbroken curves persist for $|\sin\chi| \to 1$ even in Fig. 5 (b); this is just the WG limit. A lesser degree of robustness is observed for the oscillatory trajectories: they are surrounded by elliptical "stable islands", but a chaotic sea forms in-between, owing to the fact that in Fig. 5 (b) the diametral separatrix orbit mentioned above is *unstable*, developing the sensitivity to small deviations in initial conditions which is typical for chaotic behavior. Chaos develops preferentially around such separatrix orbits. The analogy to a pendulum makes this plausible: there, the separatrix is the unstable equilibrium point at which the pendulum balances upside down. Note that the different types of motion described here are *mutually exclusive*, i.e. chaotic orbits never cross over into the islands of stability. This has the important effect that chaotic motion is indirectly affected by the presence of stable structure in the SOS.

The central reason why the SOS is introduced in this chapter is that it allows us to form a bridge between the discrete electromagnetic modes of the cavity and their measurable emission characteristics. Emission means coupling to the environment and hence appears as a dissipation mechanism in the internal cavity dynamics, as illustrated in Eq. (9). Recalling section 2, the emission from a dielectric cavity is governed foremost by Fresnel's formulas, which give a wavelength-independent relation for the reflectivities r_ν along any ray path, determined only by the local angle of incidence χ_ν at reflection ν; in the example of the Fabry-Perot cavity, nothing else is needed to determine the decay rate γ of a cavity mode, cf. Eq. (8). Now we note that the SOS shows the angle of incidence on the vertical axis, and hence the Fresnel coefficient of any given reflection can be read off with ease. In particular, the critical angle for TIR, Eq. (1), is represented in the SOS as a horizontal line. When this line is crossed from above (in absolute value), refractive escape becomes possible. The SOS then tells us which combinations of initial conditions give rise to ray trajectories that eventually reach this classical escape window in phase space.

12 Uncertainty principle

To complete the bridge between a cavity mode and its corresponding set of initial conditions in the ray dynamics, we have to find a way of projecting quasibound fields onto the

SOS. To this end, let us briefly discuss some aspects of how mode fields can be measured. Individual quasibound states can be studied in great detail in *microlaser* experiments [96, 97, 16, 98], because one can make spatially and spectrally resolved images of the emitter under various observation angles. As is evident from Fig. 4, the far-field intensity depends on the polar angle θ of the detector relative to some fixed cross-sectional axis of the object (say, the horizontal axis). Instead of simply measuring this far-field intensity, however, one can also ask from which points on the cavity surface the collected light originated – i.e., an *image* of the emitter can be recreated with the help of a lens. The dielectric will then exhibit bright spots at surface locations ϕ whose distribution in the image may change as a function of observation angle θ. The two variables ϕ and θ are conjugate to each other, because θ measures a propagation *direction* whereas ϕ is a position coordinate of the cavity.

The conjugacy between ϕ and θ means that they are *incompatible*, in the sense that they obey an *uncertainty relation*: the field distribution as a function of ϕ in the image can be deduced from the far-field distribution in θ by a Fourier transformation, and that is the function performed by the imaging lens. But quantities related by Fourier transformation cannot simultaneously have arbitrarily sharp distributions. Physically, in an image-field measurement a large lens is needed to get good spatial (ϕ) resolution, but this leaves a larger uncertainty about the direction θ in which the collected light was traveling [98].

If we could plot the measured intensity as a function of both ϕ and θ, we could generate a two-dimensional distribution similar to the SOS of the preceding ray analysis. In fact, knowing the surface shape, it is only a matter of trigonometry and the law of refraction to transform the pair (ϕ, θ) measured on the outside to (ϕ, χ) inside the cavity and hence make the analogy complete. But if one has already calculated the wave field of a quasibound state, what is the advantage of representing it in this *phase space* rather than in real space? The answer is that the real-space wave patterns often obscure information about the *correlations* between the two conjugate variables $(\phi, \sin\chi)$. As mentioned above, the SOS which plots these variables would allow us to understand whether a given mode is allowed to emit refractively; and if so, we can furthermore determine at what positions on the surface and in which directions the escape will preferentially occur. This is determined by the joint distribution of $(\phi_\nu, \sin\chi_\nu)$ over all reflections ν encountered by the rays corresponding to the given mode [51].

13 Husimi projection

To begin a phase space analysis, we now return to the question of how to extract correlations between conjugate variables from a wave field. This can be illustrated by analogy with a musical score: any piece of music can be recorded by graphing the sound amplitude as a function of time. On the other hand, musical notation instead plots a sequence of sounds by simultaneously specifying their pitch and duration. These are conjugate variables because monochromatic sounds require infinite duration [99], but their joint distribution is what makes the melody. The reason why musical scores can

be written unambiguously is that they apply to a short-wavelength regime in which the frequency smearing by finite "pulse" duration goes to zero (in this sense, all music is "classical"...). In the same way that musical notes are adapted to our perception of music, phase-space representations of optical wave fields project complex spatial patterns onto classical variables relevant in measurements.

This reasoning is familiar from quantum optics as well: there, amplitude and phase of the electromagnetic field are conjugate variables, and their joint distribution is probed in correlation experiments [100, 101]. A possible way of obtaining a phase-space representation is the *Husimi function*, obtained by forming an overlap integral between the relevant quantum state and a *coherent state* corresponding to a minimum-uncertainty wavepacket in the space of photon number versus phase. Here, we want to extract the same type of information about the joint distribution of the conjugate variables $\phi, \sin\chi$ relevant to an optical imaging measurement on a cavity mode, as described above. By projecting the electromagnetic field onto the SOS, measurable correlations are revealed which can be compared to the classical phase space structure. This is another realization of a Husimi function; the examples mentioned above differ essentially only in the actual definition of the coherent state basis onto which the wave field is projected [102].

Motivated by the above remarks on measurement of emission locations versus detector direction, we now note that the coherent states with which the cavity modes should be overlapped are in fact the *Gaussian beams* [2]. The fundamental Gaussian beam ψ_G has the property of being a minimum-uncertainty wavepacket in the coordinate x transverse to its propagation direction z, evolving according to the paraxial (Fresnel) approximation in complete analogy with a Schrödinger wavepacket,

$$\psi_G(x,z) = \frac{1}{(2\pi)^{1/4}} \frac{1}{\sqrt{\sigma + \frac{i\,z}{2k\sigma}}} \exp\left[-\frac{x^2}{4\sigma^2 + 2iz/k}\right] \exp(ikz). \tag{32}$$

The "waist" of the beam at $z = 0$ is σ, and the *angular beam spread* is

$$\Delta\theta = \arctan\left(\frac{1}{k\,\sigma}\right) \approx \frac{1}{k\,\sigma}. \tag{33}$$

In the imaging setup, σ determines the spatial resolution. Only beams with angular spread smaller than a maximum $\Delta\theta$ are admitted by the aperture, and hence features smaller than the corresponding σ are unresolved. Clearly, the uncertainty product $\sigma\,\Delta\theta$ vanishes for high wavenumbers.

We are concerned with the *internal* cavity, and thus do not want the definition to contain the particular leakage mechanism (e.g., the law of refraction). Therefore, imagine that our detector could be placed *inside* the cavity, close to its boundary. Given the internal field ψ_{int} of the mode, we then make a hypothetical measurement by forming the overlap with a minimum-uncertainty wavepacket ψ_G of width σ, centered around a certain value of ϕ and $\sin\chi$. The form of ψ_G is analogous to Eq. (32), but transformed to polar coordinates because our position variable is an angle, ϕ. The radial coordinate can be eliminated because we constrained our detector to lie on the cavity surface.

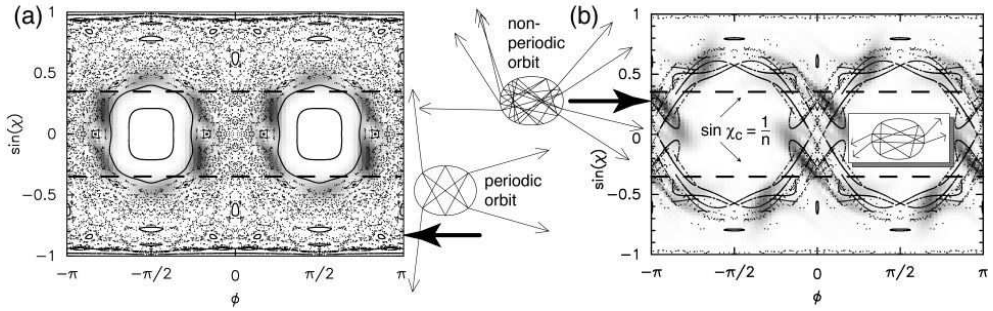

Figure 6: The Husimi projections of states (b) and (d) in Fig. 4 are shown in (a) and (b), resp., as grayscale images (dark for high intensity) superimposed onto the SOS. In (a), the field is localized in the chaotic boundary layer of the bouncing-ball island, with strong maxima on an unstable periodic orbit. Its star shape is shown in the bottom center inset, displaying ray escape according to Snell's law is as thin arrows. In (b), the cavity is the same as in Fig. 5 (b), but the SOS shows a different set of ray trajectories, forming a homoclinic tangle (interweaving black lines). The rightmost inset shows the unstable periodic orbit from which the tangle emanates. Its invariant manifolds guide the transport of phase-space density to the refractive escape window, $|\sin\chi| < 1/n \approx 0.377$ (dashed horizontal lines).

Although individual Gaussian wavepackets are not good solutions of the wave problem inside the cavity, they are *always* an allowed (though overcomplete) basis in which the field can be expanded. This is all we require in order to obtain the desired, smoothed phase space representation of $\psi_{\rm int}$: The value of the overlap integral,

$$H(\phi, \sin\chi) \equiv |\langle \psi_{int} | \psi_G \rangle|^2 \,, \tag{34}$$

as a function of ϕ and $\sin\chi$ can (with some caveats) be interpreted as a phase space density, and is the desired Husimi projection; the parameter σ in Eq. (32) should be chosen so as to optimize the desired resolution in ϕ and $\sin\chi$, i.e., the "squeezing" of the minimum-uncertainty wavepackets which probe ψ_{int}. Details on the definition, properties and applications of Husimi functions on the ray phase space are found in Refs. [8, 103, 104, 105, 107, 97]. The price we pay for obtaining a quasi-probability distribution is that Eq. (34) discards all phase information.

Figure 6 shows how the prescription Eq. (34) maps the mode of Fig. 4 (c) and (d) onto the classical ray dynamics. Although the chaotic trajectories corresponding to (d) show some accumulation near certain paths in real space, only the Husimi plot reveals what *combinations* of ϕ and $\sin\chi$ occur in the internal field. This in turn determines at what positions refractive ray escape is expected, and in which directions the light will radiate.

14 Constructive interference with chaotic rays

In this section, we return to the "mystery of the missing modes" with which section 8 confronted us: Weyl's density of states is asymptotically the same for all cavities of the same volume, even if we cannot classify their modes according some numbering that follows from integrability, or at least paraxiality. Figure 4 shows that a given mode does not cease to exist as integrability is destroyed with increasing ϵ, but evolves smoothly into a new and complex field pattern with a well-defined spectral peak that can even become narrower with increasing chaos in the ray dynamics. As noted in section 10, the "mystery" is how at large shape deformation the increasingly numerous chaotic rays, which crisscross the cavity in a pseudo-random way and even diverge from each other, can give rise to constructive interference, and hence to a resonant mode.

In section 9, the quasiclassical quantization approach led from the ray picture to the wave fields. Now, we follow the opposite direction and use the Husimi projection of a given cavity mode to perform a "dequantization" which leads to the ray picture. In this way, the novel physics of chaotic modes can be described without much technical detail.

By superimposing the Husimi projection of a mode onto the SOS for the same deformation, we can identify classical structures on which the mode is built. We have so far encountered two types of structure, cf. the caption of Fig. 5: *(I)* invariant curves such as those formed by WG rays, permitting EBK quantization as discussed in section 9; *(II)* stable islands around periodic orbits, for which the paraxial approximation of the previous chapter [86] can be used. In both cases, a finite (and usually small) number of wavefronts suffices to achieve the constructive interference without which no cavity mode can form. The mode shown in Fig. 6, on the other hand, overlaps with neither of these non-chaotic phase-space components; it is a *chaotic* mode. One possible way to understand that chaotic modes are possible at all, is to realize that even the chaotic sea is *not* structureless.

The classical objects of crucial importance for an understanding of chaotic modes are the *unstable* periodic orbits of the cavity. They give rise to a third type of invariant sets in the ray dynamics: *(III) stable and unstable manifolds*. These are one-dimensional curves which, like the structures *(I)* and *(II)*, have the property that rays launched anywhere on the manifold will always remain there. Along these manifolds, trajectories rapidly approach or depart from a given periodic orbit, such as the one shown in Fig. 6 (b, right inset). A non-periodic ray trajectory which moves along one of the corresponding manifolds is displayed in the top center inset.

The stable and unstable manifolds form an intricate web, the "homoclinic tangle", which was already recognized by Poincaré as the cause of severe difficulties in calculating the dynamics [5]. Part of this tangle is shown in Fig. 6 (b), forming interweaving lobes which play an important role in controlling the transport of phase-space density. A discussion of this "turnstile" action and the relation to the stability of the orbits from which the tangle originates is found, e.g., in Refs. [1, 108]). As the Husimi projection in Fig. 6 (b) shows, the wave intensity is guided along the invariant manifolds of the unstable periodic orbit [110], imparting a high degree of anisotropy onto the internal intensity and on the emission directions.

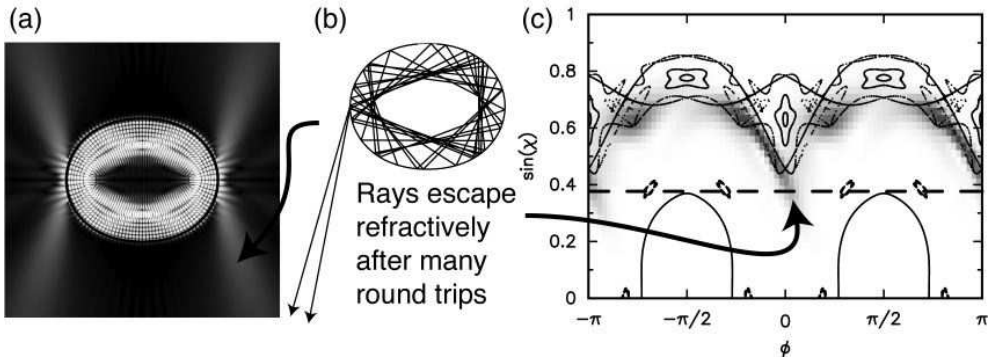

Figure 7: A WGM in the quadrupole cavity at $\epsilon = 0.104$, at dimensionless wavenumber $kR = 32.695$ and width $\kappa R = 0.0025$. The focused near-tangential emission from the points of highest curvature is explained in the ray picture (b). The ray-wave connection is illustrated in the Husimi plot (c), superimposed onto the SOS (only $\sin\chi > 0$ is plotted to magnify details). The stable and unstable manifolds of the rectangular periodic orbit funnel the rays downwards to the escape condition along two narrow pathways. The resulting emission therefore is not attributable to a single periodic orbit, but to a family of (generally aperiodic) trajectories following the invariant manifolds shown here.

Particularly strong Husimi intensity is found at the reflection points of the periodic orbit shown in the inset to Fig. 6 (b); this corresponds to the high-intensity ridges in the real-space intensity of Fig. 4 (d). Such *wavefunction scarring* [109] is a surprising feature, because a wave field concentrated near the origin of the homoclinic tangle, i.e., at the unstable periodic orbit itself, spatially appears similar to a sequence of Gaussian beams, despite the fact that paraxial optics requires the underlying modes to be *stable*. Even if we do not start from this paraxial point of view, but follow the historical developments in quantum chaos, scars seem to run counter to the early conventional wisdom that asserted chaotic modes should posses a random spatial distribution [108]. In a recent study on lasing in a large, planar laser cavity with no stable ray orbits [111], laser operation with focused emission was observed and explained by wave function scarring. This phenomenon is of interest not only from the applied point of view, but also because a complete understanding of the quasiclassical theory for modes corresponding to the invariant manifolds of type *(III)* is as yet missing [112, 113].

15 Chaotic whispering-gallery modes

The lifetime of the quasibound states in Fig. 4 (d) yields a Q-factor of $Q \equiv k/\kappa = 700$, which is of the same order as that of a high-power microlaser [97] that was demonstrated recently as an application of cavity design using the concepts introduced in section 11. The bowtie-shaped mode encountered there was of paraxial type, centered around a stable periodic ray orbit. If low lasing thresholds and hence higher Q-factors are desired, we recall from Fig. 2 that WGMs are preferred. As shown in Fig. 7, WGMs in partially

chaotic cavities display high Q *and* strongly anisotropic emission patterns. Comparing the non-chaotic case of Fig. 2 (a) and the chaotic cavity of Fig. 7, we indeed find stronger focusing in the latter case.

Chaotic WGMs are among the few types of chaotic modes for which an approximate quasiclassical description along the lines of section 9 is possible. They correspond to ray trajectories which are part of the chaotic sea but circulate along the cavity perimeter many times before exploring other phase-space regions, cf. Fig. 5 (b), bottom. There is thus a *separation of time scales* between the fast WG circulation and a slow deviation from WG behavior which inevitably ends in chaotic motion. This makes it possible to use an adiabatic approximation [114] in which the "diffusion" away from WG motion is neglected for times long enough to contain many round-trips of the ray.

As a consequence, one can formulate approximate quantization conditions for chaotic WG modes by ignoring the chaotic dynamics [51], leading to equations of the EBK type, Eq. (30). The approximate nature of this quantization can be recognized in Fig. 7 (a), which differs from the ellipse-shaped cavity of Fig. 2 (a) in the fact that a small but nonvanishing field persists in the cavity center. This indicates that there no longer is a well-defined caustic, as we required in section 9 Nevertheless, the Husimi distribution (grayscale) in Fig. 7 (c) condenses approximately onto a one-dimensional curve (the shape of which can be given analytically within the adiabatic approximation [51]), following the homoclinic tangle [the SOS in Fig. 7 (c) is vertically expanded compared to Fig. 6 (b)]. The location of this *adiabatic invariant curve* is determined by the EBK quantization; its minima are seen to approach the TIR condition.

As indicated in section 14, chaos does become important when the emission properties of a chaotic WG mode are concerned. It is the deviation of the rays from the above adiabatic assumption which allows an initially confined ray to violate the total-internal reflection condition after some time, and hence escape refractively, cf. Fig. 7 (b). In Fig. 7 (c), this escape results from wave intensity leaking across the TIR condition near $\phi = 0, \pi$. This can be reproduced within a ray simulation by launching an ensemble of rays on the adiabatic invariant curve, and recording the distribution of classically escaping rays.

This implements the program outlined at the end of section 4 The stochastic branching of a ray trajectory into transmitted and reflected parts, also known as ray-splitting [48], could be summed up as a geometric series in the Fabry-Perot example, Eq. (6). In the oval cavity, Monte-Carlo simulations for large ensembles of incident rays are required [51]. This ray approach has been applied in scattering problems along the lines of Eq. (10) [49]; the value and applicability of ray considerations in scattering from *chaotic* optical cavities was demonstrated in Ref. [50]. The difference to the *quasibound-state* approach is that our incident rays are launched inside the cavity, not outside of it.

Because chaotic diffusion makes classical escape from WGMs possible in the first place, the ray approach in fact becomes more useful at large deformations where chaos increases. That is just the regime where exact scattering calculations encounter difficulties. Starting from the ray approach to emission directionality and decay rates, one can then successively introduce corrections at higher orders in λ. In particular, in Ref. [51], the openness of the system was taken into account in the semiclassical quantiza-

tion step by introducing additional phase shifts into the EBK equations. The reason is that penetration into the outside region, as mentioned in section 2, creates an enlarged, effective cavity boundary which lengthens the ray path lengths. This "Goos-Haenchen effect" [15] is well-known from plane interfaces as well. The effective cavity is actually of slightly different shape than the physical geometry. This has the consequence that *even the elliptic* cavity of Fig. 2, which for impenetrable boundaries is integrable, becomes non-integrable as a dielectric body [46, 47].

16 Dynamical eclipsing

In the $\lambda \to 0$ limit, the internal dynamics of the ellipse displays no chaos, cf. Fig. 5 (a). This makes it an important test case with which to compare whenever we want to identify fingerprints of chaos. The power of such comparisons has been illustrated in an experiment on prolate, dye-doped lasing microdroplets [98]. The geometry of the droplets was rotationally symmetric around the polar axis, which is also the major axis. If one analyzes only the light propagating in a plane containing the two poles, then the cavity is effectively formed by the 2D axial cross section whose shape is an oval of the type we have been discussing above, cf. Fig. 5. The experimental technique of recording with a CCD camera an image of the micro-object at various observation angles θ (measured with respect to the polar axis of a spheroidal droplet) reveals prominent bright and dark regions along the cavity rim, from which the position and exit angle of the laser emission can be extracted simultaneously.

As discussed in section 3, the lasing modes in low-index materials such as droplets should be of WG-type. The experiment illustrates both the focusing property, as well as the robustness of WGMs. When the lasing droplets are imaged from the side perpendicular to the polar axis ($\theta = 90°$), one thus expects emission directionality of the type shown in Figs. 2 (a) or 7 (a), showing emission from the points of highest curvature (i.e., the poles). However, *neither* case describes the observed emission correctly. The droplets appeared dim at the poles instead of being brightest there.

This counter-intuitive phenomenon can be explained by the phase space structure shown in Fig. 5 (b). An essential role is played by the small islands belonging to the stable four-bounce diamond-shaped orbit depicted in the Figure. Its effect is that WG rays of the type shown below the SOS are prevented from reaching the high-curvature points ($\Phi = 0,\ \pi$) at angle of incidence $\sin\chi = 0.65$, because chaotic and stable motion are mutually exclusive (cf. section 11). Now $\chi_{\rm TIR} = \arcsin 0.65$ just happens to be the critical angle for the droplet-air interface; hence, near-critical escape from the highest-curvature points is ruled out for chaotically moving WG rays in the droplet. In Fig. 5 (b), it is impossible to see from the ray trace in real space that the combination $\phi = 0$, $\chi = \chi_{\rm TIR}$ will never occur. Likewise, this information is by no means obvious from the wave equation itself Only the phase-space analysis using the SOS reveals the small islands that cause this effect, which has been called *dynamical eclipsing*. The emission profile is determined by the phase space structure in the vicinity of the emission line $\sin\chi_{TIR}$, and therefore we do not detect dynamical eclipsing in the higher-index example

of Fig. 7. A glance at Fig. 5 (a) makes it clear that the effect will never occur in the ellipse, because the relevant islands do not exist there.

17 Conclusions

The subtle difference in shapes between ellipsoid and quadrupole raises the question: *How short does the wavelength have to be compared to the cavity dimensions, in order to be able to resolve such differences in geometry?* Clearly, the droplets are so large compared to the optical wavelength (35 μm diameter for an equivalent-volume sphere) that we are deep in the short-wavelength limit. What the above example teaches us is that it is not the structure in real space that has to be resolved by the waves, but the structure in phase space. The uncertainty principle will limit the size of the islands that can have a noticeable effect on the cavity mode structure, but the important thing to realize is that small differences in cavity shape can lead to large differences in phase space structure. As a result, the phase space effects introduced in this chapter turn out to be observable even in cavities that are not much larger than the wavelength. This is an extension of the claim made for integrable systems in section 9, that quasiclassical methods often extend all the way to the longest-wavelength modes.

Future work on nonintegrable dielectric cavities can proceed in various directions: our understanding of the *classical* ray transport in partially chaotic systems has to be explored further, and the systematic *wave* corrections to these ray ideas must be investigated. Two such corrections which are of particular importance in chaotic systems are dynamical localization [114, 51, 115] and chaos-assisted tunneling [107]. Dynamical localization is an interference effect that suppresses decay rates below the value expected from ray simulations as outlined in this chapter. It becomes more pronounced in smaller cavities, and in fact helps maintain high Q-factors in the presence of chaotic ray dynamics. Localization arises in many areas of physics as a name for wave corrections to a classical diffusion picture. In our case, the diffusion happens in the chaotic phase space of the ray dynamics. Chaos-assisted tunneling, on the other hand, acts to enhance radiation losses of *non-chaotic* WGMs at small deformations when chaos pervades only the low-$\sin\chi$ regions of the SOS. It also leads to a coupling between WG wavefronts encircling the cavity in counterclockwise and clockwise sense of rotation, e.g., between the extreme bottom and top of the SOS in Fig. 4 (a). In the ray picture, spontaneous reversal of rotation direction is forbidden for WG trajectories on invariant curves; the mechanism at work here is tunneling in phase space.

The phase space approach to microcavity electrodynamics provides a means of classifying the wide variety of modes in cavities where "good quantum numbers" do not uniquely enumerate the spectrum. Semiclassical methods provide the connection between individual modes and manifolds in phase space, such as the caustics in section 9, belonging to invariant curves in the SOS. Open questions remain about how to establish this connection in the general case when caustics are broken up by ray chaos. The particularly important case of WGMs, however, is amenable to approximate treatments which permit quantitative predictions. Many systems in which strong matter-field cou-

pling enables quantum-electrodynamic studies, are actually large enough to be in the quasiclassical regime: examples are semiconductor domes [90] (where the effective wavelength is shortened by a high refractive index), or silica microspheres (cf. Ref. [21, 23] and citations therein) where atoms close to the dielectric interface interact evanescently with WGMs whose angular momentum according to Eq. (31) is $m \sim 10^3$. At all levels of microcavity optics – quantum or classical, linear or nonlinear – the fundamental task is to establish a modal basis, and the methods we sketched in this chapter accomplish this in a way that provides physical insight.

References

[1] Reichl, L. E. (1992). "The Transition to Chaos in Conservative Classical Systems: Quantum Manifestations," Springer-Verlag, New York

[2] Siegman, A. E. (1986). "Lasers," University Science Books, Mill Valley, CA

[3] Gutzwiller, M. C. (1998). Resource Letter ICQM-1: The interplay between classical and quantum mechanics. *Am. J. Phys.* **66**, 304

[4] Heller, E. and Tomsovic, S. (1993). Post-modern quantum mechanics. *Physics Today* **46**, 38.

[5] Gutzwiller, M. C. (1990). "Chaos in Classical and Quantum Mechanics," Springer Verlag, New York.

[6] Child, M. S. (1991). "Quasiclassical Mechanics with Molecular Applications," Clarendon Press, Oxford.

[7] Brack, M., and Bhaduri, R. K. (1997). "Quasiclassical Physics," Frontiers in Physics **96**, Addison-Wesley, Reading, USA.

[8] Smilansky, U. (1995). *In*: "Proc. 1994 Les Houches Summer School LXI on Mesoscopic Quantum Physics," (E. Akkermans, G. Montambaux, J. L. Pichard and J.Zinn-Justin, Ed.) p. 373. Elsevier, Amsterdam.

[9] Stöckmann, H. J. (1999) "Quantum Chaos – an Introduction," Cambridge University Press.

[10] Strutt, J. W., and Baron Rayleigh (1945). "The Theory of Sound," Vol.II. Dover Publications, New York.

[11] Anderson, J. S., and Bratos-Anderson, M. (2000). Acoustic coupling effects in St. Paul's Cathedral, London. *J. Sound Vibr.* **236**, 209.

[12] Pipino, A. C. R. (1999). Ultrasensitive surface spectroscopy with a miniature optical resonator. *Phys. Rev. Lett.* **83**, 3093.

[13] Johnson, B. R. (1993). Theory of morphology-dependent resonances: shape resonances and width formulas. *J. Opt. Soc. Am.* **10**, 343.

[14] Nöckel, J. U., and Stone, A. D., *In* " Optical Processes in Microcavities", (R. K. Chang and A. J. Campillo, Eds.). World Scientific, Singapore.

[15] Snyder, A. W., and Love, J. D. (1991). "Optical Waveguide Theory,". Chapman and Hall, London.

[16] Braun, I., *et al.* (2000). Hexagonal microlasers based on organic dyes in nanoporous crystals. *Appl. Phys. B* **70**, 335.

[17] Kerker, M. (1969). "The Scattering of Light and Other Electromagnetic Radiation," Academic Press, New York.

[18] v.d.Hulst, H. C. (1957). "Light scattering by small particles," Wiley, New York.

[19] Nussenzveig, H. M. (1969). High-frequency scattering by a transparent sphere. I. Direct reflection and transmission. *J. Math. Phys.* **10**, 82

[20] Barber, P. W. and Hill, S. C. (1990). "Light Scattering by Particles: Computational Methods," World Scientific, Singapore.

[21] Sandoghdar, V., *et al.* (1996). Very-low threshold whispering-gallery microsphere laser. *Phys. Rev. A* **54**, R1777.

[22] Vernooy,D. W., *et al.* (1998). Cavity QED with high-Q whispering-gallery modes. *Phys. Rev. A* **57**, R2293.

[23] Kuritzki, G., *et al.* (2000). Control of atomic-state decay in cavities and microspheres. *New J. Phys.* **2**, 1.

[24] Schmitt, C. G., and Arnott, W. P. (1999). Infrared emission (500-2000 cm^{-1}) of laboratory ice clouds. *J. Quant. Spectr. Rad. Trans.* **63**, 701

[25] Fields, M., Popp, J., and Chang, R. K. (2001). *In* "Progress in Optics," (E. Wolf, Ed.), p.1. Elsevier Science Publishers.

[26] Yamamoto, Y., Slusher, R. E. (1993). Optical processes in microcavities. *Physics Today* **46**, No. 6, 66.

[27] Chang, S. S. *et al.*, (1999). Stimulated emission and lasing in whispering-gallery modes of GaN microdisk cavities. *Appl. Phys. Lett.* **75**, 166.

[28] Nöckel, J. U. (2001). Optical feedback and the coupling problem in semiconductor microdisk lasers. submitted to *physica status solidi*.

[29] Roll, G., and Schweiger, G. (1998). Resonance shift of obliquely illuminated dielectric cylinders: geometric-optics estimates. *Appl. Opt.* **37**, 5628.

[30] Poon, A. W., Chang, R. K., and Lock, J. A. (1998). Morphology-dependent resonances in an optical fiber: effects of fiber tilt and focused Gaussian beam illumination. *Opt. Lett.* **23**, 1105.

[31] Artemyev, M. V., Woggon, U. and Wannemacher, R. (2001). Photons confined in hollow microspheres. *Appl. Phys. Lett.* **78**, 1032.

[32] Mazumder, M. M., Hill, S. C., and P. W. Barber (1992). Morphology-dependent resonances in inhomogeneous spheres – comparison of the layered T-matrix method and the time-dependent perturbation method. *J. Opt. Soc. Am. A* **9**, 1844; Chowdhury, D. Q., Hill, S. C., and Barber, P. W. (1991). Morphology-dependent resonances in radially inhomogeneous spheres, *J. Opt. Soc. Am. A* **8**, 1702

[33] Chin, M. K., *et al.* (1999). GaAs microcavity channel-dropping filter based on a race-track resonator. *IEEE Photon. Technol. Lett.* **11**, 1620.

[34] Benson, T. M., and Kendall, P. C. (1995). *In* "Methods for Modeling and Simulation of Guided-Wave Optoelectronic Devices: Part I, PIER 10," (W. P. Huang, Ed.). EMW Publishing, Cambridge

[35] Lee, K. M., Leung, P. T., and Pang, K. M. (1998). Iterative perturbation scheme for morphology-dependent resonances in dielectric spheres. *J. Opt. Soc. Am. A* **15**, 1383.

[36] Fan, X. D., *et al.* (2000). Coupling semiconductor nanocrystals to a fused-silica microsphere: a quantum-dot microcavity with extremely high Q-factors. *Opt. Lett.* **25**, 1600.

[37] Waalkens, H., Wiersig, J., and Dullin, H. R. (1997). Elliptic quantum billiard. *Ann. Phys.* **260**, 50

[38] Landau, L. D., and Lifshitz, E. M. (1979). "Quantenmechanik," Akademie-Verlag Berlin.

[39] Lazutkin, V. F. (1993). "KAM Theory and quasiclassical Approximations to Eigenfunctions," Springer, New York.

[40] Blatt, J. M., and Weisskopf, V. F. (1952). "Theoretical Nuclear Physics," Wiley, New York.

[41] Xu, Y., Lee, R. K., and Yariv, A. (2000). Scattering-theory analysis of waveguide-resonator coupling. *Phys. Rev. E* **62**, 7389.

[42] Taylor, J. R., (1972). "Scattering Theory," Wiley, New York.

[43] Eckhardt, B. (1988). Irregular scattering. *Physica D* **33**, 89.

[44] Blümel, R., and Smilansky, U. (1988). Classically irregular scattering and its quantum mechanical implications. *Phys. Rev. Lett.* **60**, 477.

[45] Miller, W. H. (1975). *In* "Advances in Chemical Physics" **30**, 77. (K. P. Lawley, Ed.) Wiley, New York.

[46] Yeh, C. (1963). Diffraction of waves by a penetrable ribbon. *J. Math. Phys.* **4**, 65.

[47] Lock, J. A., *et al.* (1998). Amplification of high-order rainbows of a cylinder with an elliptical cross section. *Appl. Opt.* **37**, 1527.

[48] Blümel, R., *et al.* (1996). Ray splitting and quantum chaos. *Phys. Rev. A* **53**, 3284.

[49] Tränkle, E., and Riikonen, M. (2000). Elliptical halos, Bottlinger's rings, and the ice-plate snow-star transition. *Appl. Opt.* **35**, 4871.

[50] Jensen, J. H. (1993). Chaotic scattering of light by a dielectric cylinder. *J. Opt.Soc. Am. A* **10**, 1204.

[51] Nöckel, J. U., and Stone, A. D. (1997). Chaotic light: a theory of asymmetric cavity resonators. *Nature* **385**, 45

[52] Hentschel, M., and Nöckel, J. U. (2001). The sequential-reflection model in deformed dielectric cavities. to be published in Proceedings of the Colloquium of the Royal Netherlands Academy of Arts and Sciences.

[53] Lamb, W. E., Schleich, W. P., Scully, M. O., and Townes, C. H. (1999). Laser physics: quantum controversy in action. *Rev. Mod. Phys.* **71**, S263

[54] Vaynsteyn, V. A. 1969). "Theory of Open Resonators and open Waveguides," Golem Press, Boulder; especially chapter 64.

[55] Moiseyev, N. (1998). Quantum theory of resonances: calculating energies, widths and cross-sections by complex scaling. *Phys. Rep.* **302**, 211.

[56] Smith, F. (1960). Lifetime matrix in collision theory. *Phys. Rev.* **118**, 349.

[57] Fyodorov, J., and Sommers, H.-J. (1997). Statistics of resonance poles, phase shifts and time delays in quantum chaotic scattering: random matrix approach for systems with broken time-reversal invariance. *J. Math. Phys.* **38**, 1918

[58] Thirring, W. (1979). " Quantum Mechanics of Atoms and Molecules" **3**. Springer, New York.

[59] Friedel, J. (1958). Metallic alloys. *Nuovo Cim. Ser. 10* Suppl. **7**,287.

[60] Krein, M. G. (1962). Perturbation determinants and formula for traces of unitary self-adjoint operators. *Sov. Math.-Dokl.* **3**, 707.

[61] Loyd, P. (1967). Wave propagation through an assembly of spheres. II The density of single-particle eigenstates. *Proc. Phys. Soc.* **90**, 207.

[62] Loyd, P., and Smith, P. V. (1972). Multiple scattering theory in condensed materials. *Adv. Phys.* **21**, 69.

[63] Faulkner, J. S. (1977). Scattering theory and cluster calculations. *J. Phys.* **C 10**, 4661.

[64] Gaspard, P. 1993). *In* Proc. of the International School of Phys. "Enrico Fermi", Course CXIX, Varena (G. Casati, I. Guarneri and U. Smilansky , Eds.). North Holland, Amsterdam.

[65] Wirzba, A., and Henseler, M. (1998). A direct link between the quantum-mechanical and semiclassical determination of scattering resonances. *J. Phys. A: Math. Gen.* **31**, 2155.

[66] Purcell, E.M. (1946). Spontaneous emission probabilities at radio frequencies. *Phys. Rev.* **69**, 681.

[67] Heinzen, D. J., *et al.* (1987). Enhanced and inhibited spontaneous emission by atoms in a confocal resonator. *Phys. Rev. Lett.* **58**, 1320.

[68] Meschede, D., (1992). Radiating atoms in confined space – from spontaneous emission to microlasers. *Phys. Rep.* **211**, 201.

[69] Matinaga, F. M., *et al.* (1993). Low-threshold operation of hemispherical microcavity single-quantum-well lasers at 4 K. *Appl. Phys. Lett.* **62**, 443.

[70] Brorson, S. D., and Skovgaard, P. M. W. (1996). *In* " Optical Processes in Microcavities," (R. K. Chang and A. J. Campillo, Eds.) World Scientific, Singapore.

[71] Hulet, R. G., Hilfer, E. S., and Kleppner, D. (1985). Inhibited spontaneous emission by a Rydberg atom. *Phys. Rev. Lett.* **55**, 2137.

[72] Yablonovic, E. (1987). Inhibited spontaneous emission in solid-state physics and electronics. *Phys. Rev. Lett.* **58**, 2059.

[73] Dittes, F.-M., Harney, H. L., and Müller, A. (1992). Non-exponential decay of a one-channel system. *Phys. Rev. A* **45**, 701.

[74] Wolf, J.-P., *et al.* (2001). Ballistic trajectories of optical wavepackets within microcavities. submitted to *Opt. Lett.*

[75] Mürtz, M., Frech, B., and Urban, W. (1999). High-resolution cavity leak-out absorption spectroscopy in the 10 μm region. *Appl. Phys. B* **68**, 243.

[76] Zhang, J.-Z., Leach, D. H., and Chang, R. K. (1988). Photon lifetime within a droplets – temporal determination of elastic and stimulated Raman scattering. *Opt. Lett.* **13**, 270.

[77] Friedrich, H. (1991). "Theoretical Atomic Physics," Springer Verlag, Berlin.

[78] Haake, F. (1992). "Quantum Signatures of Chaos," Springer, Berlin.

[79] Kohler, A., and Blümel, R. (1998). Weyl-formulas for quantum ray-splitting billiards. *Ann. Phys.* **267**, 249.

[80] Balian, R., and Bloch, C. (1970). Distribution of eigenvalues for the wave equation in a finite domain. I. Three-dimensional problem with smooth boundary surface. *Ann. Phys.* **60**, 401.

[81] Yariv, A. (1975). "Quantum Electronics," John Wiley, New York.

[82] Weyl, H. (1968). "Gesammelte Abhandlungen," Springer Verlag, Berlin.

[83] Kac, M. (1966). Can one hear the shape of a drum? *Am. Math. Monthly* **73**, 1.

[84] Eckhardt, B. (1988). Quantum mechanics of classically non-integrable systems. *Phys. Rep.* **163**, 205.

[85] Laeri, F., and Nöckel, J. U. (2001). *In* "Handbook of Advanced Electronic and Photonic Materials" (H. S. Nalwa, Ed.) Academic Press, San Diego.

[86] Siegman, A. E., previous chapter in this volume

[87] Babič, V. M., and Buldyrev, V. S. (1972). "Short-Wavelength Diffraction Theory," Springer-Verlag, Berlin.

[88] Keller, J. B., and Rubinow, S. I. (1960). Asymptotic solution of eigenvalue problems. *Ann. Phys.* **9**, 24.

[89] Roll, G., and Schweiger, G. (2000). Geometrical optics model of Mie resonances. *J. Opt. Soc. Am. A* **16**, 882.

[90] Nöckel, J. U., *et al.* (2000). Mode structure and ray dynamics of a parabolic-dome microcavity. *Phys. Rev. E* **62**, 8677.

[91] Richens, P. J., and Berry, M. V. (1981). Pseudointegrable systems in classical and quantum mechanics. *Physica* **2D**, 495.

[92] Einstein, A. (1917). Zum Quantensatz von Sommerfeld und Epstein. *Verh. Deut. Phys. Ges.*

[93] Arnol'd, V. I. (1989). " Mathematical Methods of Classical Mechanics, " Springer, New York.

[94] Zaslavsky, G. M. (1999). Chaotic dynamics and the origin of statistical laws. *Physics Today* **52** No. 8, 39.

[95] Goldstein, H. (1980). "Classical Mechanics," 2nd ed. Addison-Wesley, Reading, MA.

[96] Mekis, A., *et al.* (1995). Ray chaos and Q-spoiling in lasing droplets. *Phys. Rev. Lett.* **75**, 2682.

[97] Gmachl, C., *et al.* (1998). High power directional emission from lasers with chaotic resonators. *Science* **280**, 1556.

[98] Chang, S. S., Nöckel, J. U., Chang, R. K., and Stone, A. D. (2000). Observation of emission from chaotic lasing modes in deformed microspheres: displacement by the stable orbit modes. *J. Opt. Soc. Am. B* **17**, 1828.

[99] Bartelt, H. O., Brenner, K.-H., and Lohmann, A. W. (1980). The Wigner distribution function and its optical production. *Opt. Commun.* **32**, 32.

[100] Walls, D. F., and Milburn, G. J. (1994). "Quantum Optics," Springer, Berlin.

[101] Raymer, M. G., Beck, M., and McAlister, D. F. (1994). Complex wave-field reconstruction using phase-space tomography. *Phys. Rev. Lett.* **72**, 1137.

[102] LeBoeuf, P., and Saraceno, M. (1990). Eigenfunctions of non-integrable systems in generalized phase-spaces. *J. Phys. A: Math. Gen.* **23**, 1745.

[103] Crespi, B., Perez, G., and Chang, S.-J. (1993). Quantum Poincaré sections for two-dimensional billiards. *Phys. Rev. E* **47**, 986.

[104] Tualle, J.-M., and Voros, A. (1995). Normal modes of billiards portraied in the stellar (or nodal) representation. *Chaos, Solit. Fract.* **5**, 1085.

[105] Frischat, S. D., and Doron, E. (1997). Quantum phase-space structures in classically mixed systems: a scattering approach. *J. Phys. A: Math. Gen.* **30**, 3613.

[106] Klakow, D., and Smilansky, U. (1996). Wave functions, expectation values and scars on Poincaré sections – a scattering approach. *J. Phys. A: Math. Gen.* **29**, 3213.

[107] Hackenbroich, G., and Nöckel, J. U. (1997). Dynamical tunneling in optical cavities. *Europhys. Lett.* **39**, 371.

[108] Bohigas, O., Tomsovic, S., and Ullmo, D. (1993). Manifestation of classical phase space structures in quantum mechanics. *Phys. Rep.* **223**, 43, and references therein.

[109] Heller, E. (1984). Bound-state eigenfunctions of classically chaotic Hamiltonian systems: scars of periodic orbits. *Phys. Rev. Lett.* **53**, 1515.

[110] Schweizer, W., Jans, W., and Uzer, T. (1998). Optimal localization of wavepackets on invariant structures. *Phys. Rev. B.* **58**, 1382.

[111] Fukushima, T., *et al.*, (1998). Beam-propagation behavior in a quasi-stadium laser diode. *Optics Express* **2**, No. 2, p.21.

[112] Tomsovic, S., and Heller, E. (1993). Quasiclassical construction of chaotic eigenstates. *Phys. Rev. Lett.* **70**, 1405.

[113] Kaplan, L. (1999). Scar and antiscar quantum effects in open quantum systems. *Phys. Rev. E* **59**, 5325.

[114] Nöckel, J. U. (2001). Angular momentum localization in oval billiards. *Physica Scripta* **T 90**, 263.

[115] Starykh, O. A., *et al.* (2000). Signature of dynamical localization in the resonance width distribution of wave-chaotic dielectric cavities. *Phys. Rev. E* **62**, 2078.